Design, Implementation, and Characterization of an Optical Power Supply Spot Array Generator for a Four Stage Free-Space Optical Backplane

Rajiv Iyer

Department of Electrical Engineering
McGill University
Montréal, Canada
March, 1997

A thesis submitted to the Faculty of Graduate Studies and Research in partial fulfillment
of the requirements of the degree of Master of Engineering

0-612-29603-2

Abstract

In order to alleviate the throughput bottlenecks being encountered by high speed electronic computing and switching systems, research is turning its attention toward free-space photonics technology. Of particular interest currently is the use of Hybrid/SEED devices implemented as smart pixel arrays to encode the electronic data onto an array of constant power beams of light.

This paper presents the design and implementation of a robust, scalable and modular optical power supply spot array generator for a modulator based free-space optical backplane demonstrator. Four arrays of 8 by 4 spots of ($1/e^2$ irradiance) 6.47μm radii pitched at 125μm in the vertical direction and 250μm in the horizontal were required to provide the light for the optical interconnect. Tight system tolerances demanded careful optical design, elegant optomechanics, and simple but effective alignment techniques. Issues such as spot array generation, polarization, power efficiency, and power uniformity are discussed and characterization results are presented.

Sommaire

Les processeurs à haute performance nécessitent d'ore et déjà d'être reliés par le biais de connections pouvant supporter des débits d'information extrêmement élevés. La technologie actuelle ne suffisant plus, l'effort de recherche se tourne vers l'utilisation de liens optiques fonctionnant à l'air libre pour remplacer les traces de cuivre actuellement utilisées. L'utilisation de puces optoélectroniques incorporant une matrice de pixels basée sur la technologie Hybrid/SEED pour moduler la lumière semble être particulièrement prometteuse.

La conception et la construction d'un module d'alimentation optique générant une matrice de faisceaux nécessaires au fonctionnement d'un démonstrateur de bus photonique fonctionnant à l'air libre est présentée. Quatre matrices de faisceaux de 6.47μm de rayon (rayon défini à $1/e^2$ d'intensité) de dimension 8 par 4 séparés de 125μm verticalement et 250μm horizontalement sont requises afin d'alimenter optiquement les quatre étages du démonstrateur. Un minutieux travail de conception optique et optomécanique fût nécessaire afin de rencontrer les exigences du système. Les notions d'efficacité et d'uniformité de puissance de la matrice ainsi que les façons de la générer seront introduites. Des résultats expérimentaux seront également présentés.

Manuscript-Based Thesis - Note for the External Examiner

The following five paragraphs have been reproduced in order to inform the external examiner of the Faculty of Graduate Studies & Research regulations:

> Candidates have the option of including, as part of the thesis, the text of one or more papers submitted or to be submitted for publication, or the clearly-duplicated text of one or more published papers. These texts must be bound as an integral part of the thesis.
>
> If this option is chosen, connecting texts that provide logical bridges between the different papers are mandatory. The thesis must be written in such a way that it is more than a mere collection of manuscripts; in other words, results of a series of papers must be integrated.
>
> The thesis must still conform to all other requirements of the "Guidelines for Thesis Preparation". The thesis must include: A Table of Contents, an abstract in English and French, an introduction which clearly states the rationale and objectives of the study, a review of the literature, a final conclusion and summary, and a thorough bibliography or reference list.
>
> Additional material must be provided where appropriate (e.g. in appendices) and in sufficient detail to allow a clear and precise judgement to be made of the importance and originality of the research reported in the thesis.
>
> In the case of manuscripts co-authored by the candidate and others, the candidate is required to make an explicit statement in the thesis as to who contributed to such work and to what extent. Since the task of the examiners is made more difficult in these cases, it is in the candidate's interest to make perfectly clear the responsibilities of all authors of the co-authored papers.

The manuscript upon which this thesis was based appears following this thesis. This manuscript was submitted to Applied Optics (Optical Society of America — OSA) in March 1997. It is currently in the process of review for acceptance for publication. A copyright waiver from Applied Optics is not necessary as per OSA publication regulations.

Acknowledgments

The author would like to extend his heartfelt gratitude to his supervisor Professor David V. Plant for his support and guidance over two years of the best education the author has ever had.

The initial design of the Optical Power Supply was done by Dr. Dominic J. Goodwill (University of Colorado), whose technical guidance proved time and again to be an invaluable resource. As well, the author would like to thank the assistance by Dr. William Robertson (Middle Tennessee State University), who designed the Multiple Phase Grating, the "heart" of the Optical Power Supply. Editorial input was generously provided by Dr. David V. Plant.

Appreciation is given to the following for their assistance: George Smith (Heriot-Watt University) who machined a subset of the optomechanics for the optical power supply, Heinz Nentwich (NORTEL) who sawed the Multiple Phase Gratings to chip level accuracy, and special thanks to Don Pavlasek and Joe Boka (McGill University) who not only machined the majority of the optomechanics for the OPS, but provided invaluable assistance in their design.

The author would also like to extend a special thanks to Frank Tooley, Mike Ayliffe, David Kabal, Yongsheng Liu, Guillaume Boisset, Fred Lacroix, and Pritha Khurana for their contributions toward this paper (translation, technical advice, assistance during experiments, analysis of data, etc.). As well, a global thanks to the entire Photonics Systems Group of McGill University for their support and patience for the time-sharing of resources, and for my occasional short fuse!

Also a very warm thanks to my parents, Balu and Gita, who have provided the best education, love, and support throughout my life, my family in Montreal: Uncle, Aunty, Tara, Vineet, Dileep, Deepa, and baby Arjun, who have kept me very well nourished (physically and spiritually) over the past two years, Saraswati, and Gurumayi Chidvilasananda.

This work was supported by the Canadian Institute for Telecommunications Research under the National Centre for Excellence program of the Government of Canada, by NSERC (#OGP0155159) and FCAR (#NC-1415). This work was also supported by the Nortel/NSERC Chair in Photonic Systems. Acknowledgment is given to the ARPA/CO-OP/Honeywell DOE Workshop for the manufacture of the multiple phase grating. The author gratefully acknowledges funding from NSERC (PSG-A).

Table of Contents

CHAPTER 1 Introduction

1.1 Motivation

Computing and switching systems these days are placing heavier demands on their supporting technology than ever before. High speed data processing and handling systems, such as ATM switches and parallel computing systems, for years have been based upon an electronic foundation. However, the call for higher bandwidth, lower power consumption, lower latency, and higher connectivity, represent a set of growing requirements that are exceeding the practical physical limitations of electronics technology, more specifically, the actual interconnects from board-to-board.

1.2 The Electronic Bottleneck

Shown below in Table T1-1 are the projections from the Semiconductor Industry Association (SIA) for silicon integrated circuits [1].

Year	Feature Size (microns)	Gates	On-Chip Clock	Off-Chip Clock	Pin-out Number (Rent's Rule)
1995	0.35	800K	200 MHz	100 MHz	980
1998	0.25	2M	350 MHz	175 MHz	1640
2001	0.18	5M	500 MHz	250 MHz	2735
2004	0.12	10M	700 MHz	350 MHz	4026
2007	0.1	20M	1GHz	500 MHz	5928

Table T1-1: Semiconductor Industry Association Projections for IC Rates

On-chip clock rates for current high-speed processor chips are typically 150MHz, resulting in huge aggregate bit rates of almost 100s of Gigabits per second (Gbps) per printed circuit board [2, 3, 4, 5]. Graph G1-1 shows the trend for aggregate throughput for several high-speed processors.

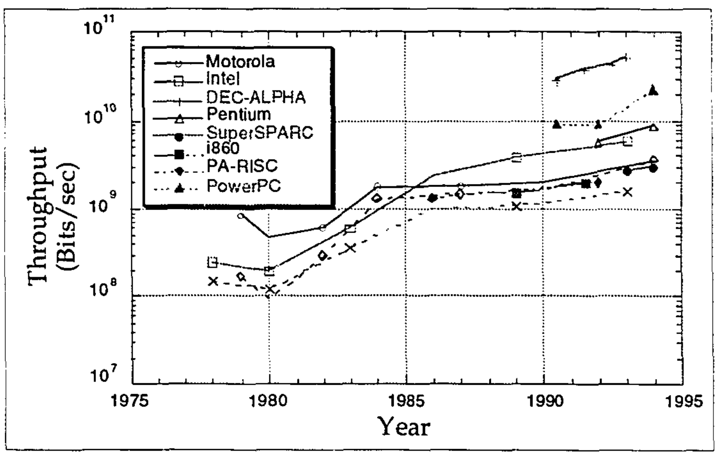

Graph G1-1: Aggregate Throughput for Selected Processors

The SIA projections indicate that with the increase of off-chip clock rates and of the number of pin-outs per chip, within a few years, aggregate data rates will be in excess of 1 Terabit per second [6]. Because the aggregate bandwidth of the integrated circuits inside these systems continues to increase, so must the capabilities of the interconnection network [7][3].

One of the fundamental problems with electrical interconnects is the bandwidth. Quantitatively, fast GaAs transistors have switching times below 10psec. However, due to parasitic effects caused by packaging, these rise and fall times increase to the order of 100psec. Once the signal is sent along the board, and then to other boards via an electrical bus within a backplane, these times increase to the order of more than 10nsec — an overall increase by 3 orders of magnitude. Other problems encountered with board-to-board electrical interconnects are power consumption (over distances of greater than 1mm), crosstalk, low fan-in and fan-out, skewing, electro-magnetic interference (EMI), ground loops, splitting losses [8], and capacitive loading effects [9].

An illustration of a typical electrical backplane is shown in figure F1-1. Printed circuit boards (PCBs) housing high-speed electronic integrated circuits (ICs) are connected to one another via an electrical bus comprised of typically 32 high speed transmission lines. The total number of lines is limited by size of the chassis, the minimum allowable line separation, and the dimensions of the electrical connectors on the PCB.

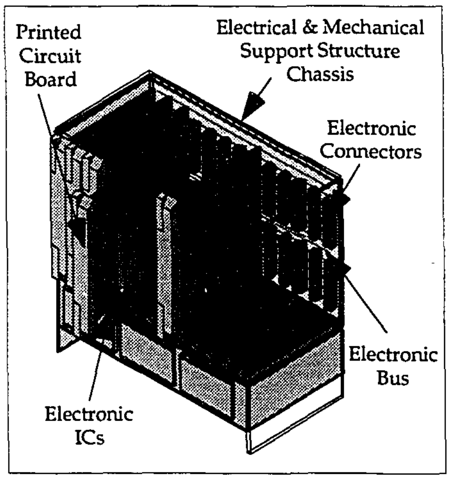

Figure F1-1: Standard Electrical Backplane

Backplane target specifications [10] forecast 1000—5000 bus connections between 10—50 boards, bit error rate of 10^{-14}, bus clock speed of 1Gb/sec, greater than 1Tbit/sec aggregate throughput, and a latency per connection of less than 2nsec. Based on the limitations of electrical backplanes, an alternative needs to be found.

1.3 The Optical Solution

The intrinsic limitations of electrical interconnection networks has led system designers to consider short-distance optical interconnects (OIs) as a way of increasing their performance [11—21]. The advantages of OIs over electrical interconnects in terms of bandwidth, connectivity, power consumption, and skew, along with some further benefits are described below.

- Electronic interconnects have a physical limit on the communication bandwidth because of the inherent resistances in the transmission line, the capacitive load, and the inductive coupling between adjacent lines and devices [9] [22]. Light, with its inherently high temporal bandwidth (of approximately 10^{14} Hz) can accommodate the projected high data rates (of approximately 10^{12} Hz).
- Exploiting the third dimension not available to electrical busses, a 2 dimensional array of optical data signals can be transmitted from board to board, increasing the connectivity of the interconnect (i.e. spatial bandwidth).
- As impedance matching and capacitive loading are no longer issues in OIs, the only power concerns deal with the optical losses within the interconnect, and electrical-to-optical and optical-to-electrical conversions in the transmitter and in the receiver respectively. [23]
- Because the speed of light is constant (3.3ps/mm), skew problems associated with variations of signal speeds in electrical connections (between 6.8 to 10.2 ps/mm) are avoided. [22]
- EMI is not a problem
- Interconnection architectural maps (e.g. fan-in, fan-out, projection, perfect shuffle) can easily be realized with simple optical components (lenses, gratings, etc.).
- Reconfigurable interconnections are simpler to design.

1.4 The Optical Backplane

The optical and optoelectronic technologies being considered for board-to-board interconnects include two-dimensional arrays of both surface-emitting and modulator-based devices integrated with arrays of electronic processing elements, called Smart Pixel Arrays (SPAs) [24]. These smart pixels can be implemented with processing electronics to build a new class of 'intelligent optical backplanes' [25]. An illustration of an optical backplane (equivalently known as a photonic backplane) is shown in figure F1-2 below.

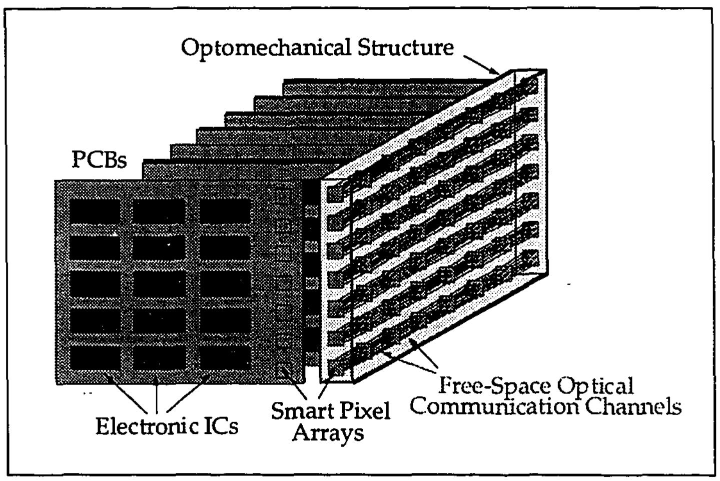

Figure F1-2: Schematic of a Optical Backplane

The current state of technology dictates that modulator based optoelectronics be used for the OIs, as the level of sophistication of large arrays of uniform surface-emitting lasers, namely Vertical Cavity Surface Emitting Lasers (VCSELs), has as yet not reached the level of adequacy to be used in these systems. A comparison between different transmitter technologies is presented in [26], and has been recently reported in [10].

A class of modulator based SPAs well suited for optical backplane interconnection applications utilizes the Hybrid/SEED technology which combines Quantum Confined Stark Effect (QCSE) modulators and PIN photodiodes (GaAs) with underlying silicon processing electronics [27] [28]. Because this type of smart pixel operates (in the transmit mode) by modulating an incident beam, systems utilizing this technology require optical power supply beams in order to power these reflective devices.

The current state of affairs shows, unfortunately, that there is a generation gap between the evolution of the sophisticated optoelectronics versus the optics necessary to drive them. Analyzing the enabling technologies required to build an optical backplane [10], it is easily seen that although optoelectronic VLSI fabrication, and transceiver circuit design is highly sophisticated, optical packaging, optomechanics, and assembly & alignment techniques are in their infancy.

1.5 Thesis Outline

Recently, the Photonics Systems Group at McGill University has constructed an optical backplane demonstration system utilizing Hybrid/SEED SPAs [15] to address the problem of bridging the generation gap that exists between optoelectronics and optics. This thesis describes the design, implementation and characterization of an optical power supply spot array generation system that was used to optically power the SPAs in a four stage free-space optical backplane. The full description of the optical design for the system was described in [29], and the optomechanical design in [30].

The paper begins by describing the requirements for the optical power supply (OPS) in Chapter 2. The light source and distribution are explained in Chapter 3. Chapter 4 describes in detail the optical design, and Chapter 5 the optomechanics. The assembly and alignment methodology, and the characterization results are provided in Chapters 6 and 7 respectively. Chapter 8 discusses some higher level issues of optical power in modulator based systems.

This paper is an elaboration of a manuscript submitted to Applied Optics (Optical Society of America) by R. Iyer, et al., [31]. Many sections have been expanded to provide mathematical justifications of models used, and to provide details on the experimental techniques employed. This thesis is written to provide a road-map for future engineers and engineering students building optical/opto-mechanical systems.

1.6 References

[1] The National Technology Roadmap for Semiconductors, Semiconductor Industry Association, (1994).

[2] T. H. Szymanski and H. S. Hinton, "Reconfigurable intelligent optical backplane for parallel computing and communications", Appl. Opt. **35**, 1253—1268, (1996).

[3] R. A. Nordin, F. J. Levi, R. N. Nottenburg, J. O'Gorman, T. Tanbun-Ek, and R. A. Logan, "A systems perspective on digital interconnections technology," J. Lightwave Technol. **10**, 811—827 (1992).

[4] T. Koinuma and N. Miyaho, "ATM in B-ISDN Communication Systems and VLSI Realization,", IEEE Journal of Solid State Circuits, **30**, 341—347, (1995).

[5] D. Bertsekas and R. Gallager, Data Networks, 2nd Ed, Prentice Hall, New Jersey, 52—56 and 128—139, (1992).

[6] H. S. Hinton and T. H. Szymanski, "Intelligent Optical Backplanes", Proceedings of the *Conference on Massively Parallel Processing with Optical Interconnects*, Oct 23-24, San Antonio, Texas, 1995.

[7] H. S. Hinton, An Introduction to Photonic Switching Fabrics, Plennum Press, NY (1993).

[8] D. H. Hartman, "Digital high speed interconnects: a study of the optical alternative", Optical Engineering, **25**, 1086—1102, (1986).

[9] A. Louri, and H. K. Sung, "3D optical interconnects for high speed interchip and intraboard communications, IEEE Computer Magazine, **27**, October 1994.

[10] D. V. Plant, "Constructing a free-space optical backplane: Challenges and choices", presented at the *Optics in Computing Meeting* at the *1997 Spring Topical Meetings*, OThB1, March 18-22, Lake Tahoe, Nevada, 1997.

[11] D. V. Plant, B. Robertson, H. S. Hinton, W. M. Robertson, G. C. Boisset, N. H. Kim, Y. S. Liu, M. R. Otazo, D. R. Rolston, and A. Z. Shang, "An optical backplane demonstrator system based on FET-SEED smart pixel arrays and diffractive lenslet arrays," IEEE Photon Tech. Lett. **7**, 1057—1059 (1995).

[12] T. Sakano, T. Matsumoto, and K Noguchi, "Three-dimensional board-to-board free-space optical interconnects and their application to the prototype multiprocessor system—COSINE-III," Appl. Opt. **34**, 1815—1822 (1995).

[13] D. Z. Tsang and T. J. Goblick, "Free-space optical interconnection technology in parallel processing systems," Opt. Eng, **33**, 1524—1531 (1994).

[14] D. V. Plant, B. Robertson, H. S. Hinton, M. H. Ayliffe, G. C. Boisset, W. Hsiao, D. Kabal, N. H. Kim, Y. S. Liu, M. R. Otazo, D. Pavlasek, A. Z. Shang, J. Simmons, and W. M. Robertson, "A 4 X 4 VCSEL/MSM optical backplane demonstrator system," in *Proceedings of the IEEE-LEOS Annual Meeting 1995* (Institute of Electrical and Electronics Engineers-Lasers and Electro-Optics Society, New York, 1995), Postdeadline paper PD2.4.

[15] D. V. Plant, B. Robertson, H. S. Hinton, M. H. Ayliffe, G. C. Boisset, D. J. Goodwill, D. N. Kabal, R. Iyer, Y. S. Liu, D. R. Rolston, W. M. Robertson, and M. R. Taghizadeh, "A multistage CMOS-SEED optical backplane demonstrator system," Opt. Comput. **96,** 14—15 (1996).

[16] F. B. McCormick, F. A. P. Tooley, T. J. Cloonan, J. L. Brubaker, A. L. Lentine, R. L. Morrison, S. J. Hinterlong, M. J. Herron, S. L. Walker, and J. M. Sasian, "Experimental investigation of a free-space optical switching network by using symmetric self-electro-optic-effect devices," Appl. Opt., **31,** 5431—5446 (1992).

[17] F. B. McCormick, T. J. Cloonan, A. L. Lentine, J. M. Sasian, R. L. Morrison, M. G. Beckman, S. L. Walker, M. J. Wojcik, S. J. Hinterlong, R. J. Crisci, R. A. Novotny, and H. S. Hinton, "Five-stage free-space optical switching network with field-effect transistor self-electro-optic-effect-device smart-pixel arrays," Appl. Opt., **33,** 1601—1618 (1994).

[18] F. B. McCormick, A. L. Lentine, R. L. Morrison, J. M. Sasian, T. J. Cloonan, R. A. Novotny, M. G. Beckman, M. J. Wojcik, S. J. Hinterlong, and D. B. Buchholz, "155 Mb/s operation of a FET-SEED free-space switching network", Photonics Technology Letters, **6,** 1479—1481 (1994).

[19] F. B. McCormick, A. L. Lentine, R. L. Morrison, J. M. Sasian, T. J. Cloonan, R. A. Novotny, M. G. Beckman, M. J. Wojcik, S. J. Hinterlong, and D. B. Buchholz, "Free-space optical switching using FET-SEED smart-pixel arrays", Inst. Phys. Conf. Ser. No 139: Part II, 131—136 (1994).

[20] D. V. Plant, B. Robertson, H. S. Hinton, W. M. Robertson, G. C. Boisset, N. H. Kim, Y. S. Liu, M. R. Otazo, D. R. Rolston, A. Z. Shang, and L. Sun, "A FET-SEED Smart Pixel Based Optical Backplane Demonstrator", Inst. Phys. Conf. Ser. No 139: Part II, 145—148 (1994).

[21] S. Araki, M. Kajita, K. Kasahara, K. Kubota, K. Kurihara, I. Redmond, E. Schenfeld, and T. Suzaki, "Experimental free-space optical network for massively parallel computers", Appl. Opt., **35,** 1269—1281 (1996).

[22] B. E. A. Saleh, M. C. Teich, Fundamentals of Photonics, Wiley and Sons, New York, Ch. 21.4, 855—871 (1991).

[23] D. Z. Tsang, "High speed optical interconnections for digital systems", The Lincoln Laboratory Journal, **4**, 31—44, (1991).

[24] T. H. Szymanski, and H. S. Hinton, "A Smart Pixel Design for a Dynamic Free-Space Optical Backplane", IEEE/LEOS Summer Topical Meeting on Smart Pixels - 94, Lake Tahoe, NV, July 11-13, 85—86(1994).

[25] H. S. Hinton, T. H. Szymanski, "Intelligent Optical Backplanes", Proceedings of the *Conference on Massively Parallel Processing with Optical Interconnections*, Oct 23—24, San Antonio, Texas, 1995.

[26] C. Fan, B. Mansoorian, D. A. Van Blerkom, M. W. Hansen, V. H. Ozguz, S. C. Esener, and G. C. Marsden, "Digital free-space optical interconnections: a comparison of transmitter technologies", Appl. Opt. **34**, 3103—3115 (1995).

[27] K. W. Goosen, J. A. Walker, L. A. D'Asaro, S. P. Hui, B. Tseng, R. Leibenguth, D. Kossives, D. D. Bacon, D. Dahringer, L. M. F. Chirovsky, A. L. Lentine, and D. A. B. Miller, "GaAs MQW modulators integrated with silicon CMOS," IEEE Photon. Technol. Lett., **7**, 360—362 (1995).

[28] D. R. Rolston, D. V. Plant, T. H. Szymanski, H. S. Hinton, W. S. Hsiao, M. H. Ayliffe, D. Kabal, M. B. Venditti, P. Desai, A. V. Krishnamoorthy, K. W. Goosen, J. A. Walker, B. Tseng, S. P. Hui, J. C. Cunningham, and W. Y. Jan, "A hybrid-SEED smart pixel array for a four-stage intelligent optical backplane demonstrator," IEEE Journal of Selected Topics in Quantum Electronics, **2**, 97—105 (1996).

[29] B. Robertson, Y. S. Liu, G. C. Boisset, D. J. Goodwill, M. H. Ayliffe, W. H. Hsiao, R. Iyer, D. Kabal, D. Pavlasek, M. R. Taghizadeh, H. S. Hinton, and D. V. Plant, "Optical design and characterization of a compact free-space

photonic backplane demonstrator," presented at the *1996 OSA Annual Meeting*, Rochester, NY, paper MLL5 (1996).

[30] G. C. Boisset, M. H. Ayliffe, D. J. Goodwill, B. Robertson, R. Iyer, Y. S. Liu, D. Kabal, D. Pavlasek, W. M. Robertson, D. R. Rolston, H. S. Hinton, and D. V. Plant, "Design, fabrication and characterization of optomechanics for a hybrid four-stage free-space optical backplane demonstrator," presented at the *1996 OSA Annual Meeting*, Rochester, NY, paper MBBB4 (1996).

[31] R. Iyer, D. J. Goodwill, W. M. Robertson, D. V. Plant, M. H. Ayliffe, G. C. Boisset, D. Kabal, F. Lacroix, Y. S. Liu, B. Robertson, "Design, Implementation, and Characterization of an Optical Power Supply Spot Array Generator for a Four Stage Free-Space Optical Backplane", manuscript submitted to Applied Optics, March 1997.

CHAPTER 2 System Overview and Optical Power Supply Requirements

In order to establish the technical context of this paper, a brief description of the system demonstrator is provided in section 2.1. With this overview, the functional utility of the OPS will have been established, resulting in a set of well defined requirements, which are presented in section 2.2.

2.1 System Overview

The system that was built by the Photonics Systems Group (McGill University) was called the Phase II demonstrator. The system was built to demonstrate the possibility and feasibility of building a complex photonic (i.e. optical & electronic) system compact and robust enough to be assembled in an industrial housing (a standard VME commercial backplane chassis) to optically interconnect four (electrical) data nodes via modulator based optoelectronics.

The four-stage system demonstrator was built in a three-dimensional layout, interconnecting four Hybrid/SEED smart pixel arrays in a unidirectional ring [1]. The chips were obtained through the ARPA/CO-OP/AT&T workshop [2] and a layout schematic of the modulators and detectors is shown in figure F2-1. Sixteen smart-pixels operating in dual-rail were arranged on the chip in interleaving columns of detectors and modulators. The modulators of the smart pixel arrays (SPAs) were laid out on an 8 by 4 grid pitched 125μm in the vertical direction and 250μm in the horizontal direction. The 32 modulator windows had a dimension of 20μm by 20μm. A full description of the chip design is given in [3]. A photograph of the Hybrid/SEED chip is shown in figure F2-2.

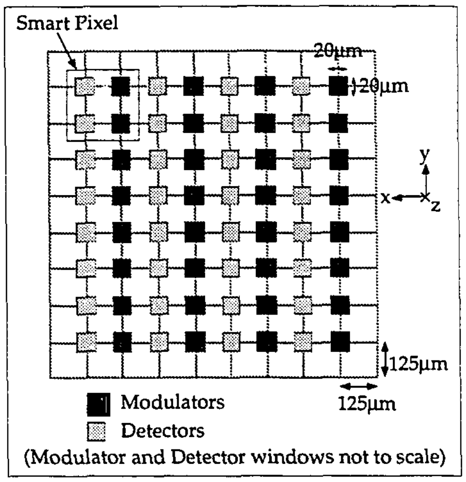

Figure F2-1: layout of the modulators and transmitters on the Hybrid/SEED chip

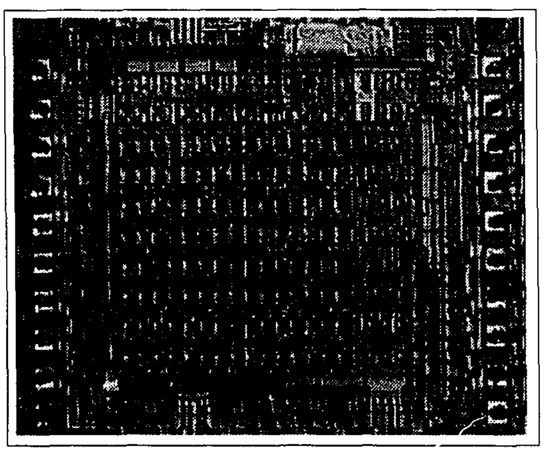

Figure F2-2: Photograph of the Hybrid/SEED Chip

A schematic of the unfolded optical layout of the system is shown below in figure F2-3. (This figure is slightly misleading since the printed circuit boards should lie in the plane of the page and the optical power supplies perpendicular to the page).

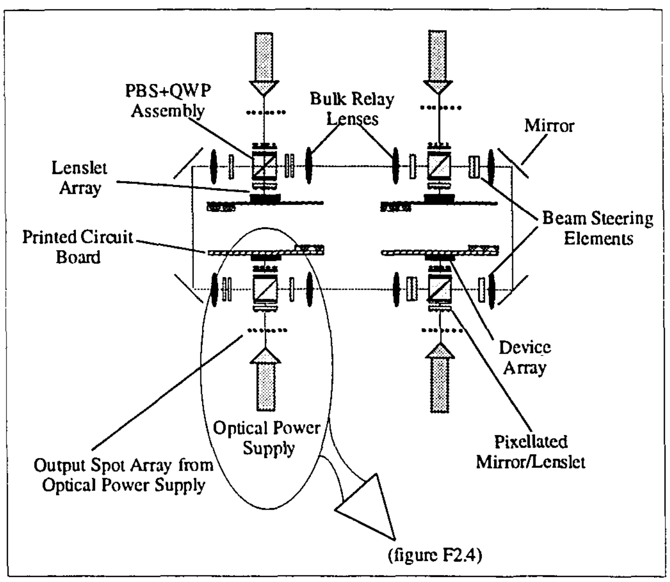

Figure F2-3: Schematic of the unfolded system

The optical interconnect was polarization based, and routed the optically encoded data from one stage to the next via polarization optics. A close-up of one stage is illustrated in figure F2-4.

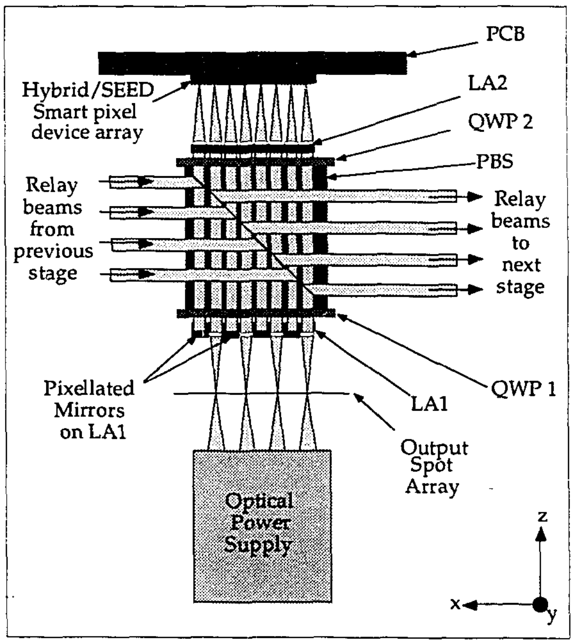

Figure F2-4: Close up of one stage

The focused spot array generated by the optical power supply was first collimated by the (125μm x 125μm) micro-lenses of the first pixelated-mirror/diffractive lenslet array (LA1). The light comprising the spot array needed to be right-hand circularly-polarized such that after passing through the first quarter-wave plate (QWP1) (oriented at 45° in the x-y plane with respect to the axis of the polarizing beam splitter (which has as yet not been introduced), it became linearly (p-) polarized. After passing through the polarizing beam splitter (PBS), and the second quarterwave plate (QWP2) (also oriented at 45^{0} in the x-y plane with respect to the axis of the PBS) which re-circularized the polarization, the beam array was then focused onto the modulators on the Hybrid/SEED smart pixel device array residing on the printed circuit board (PCB) by the second diffractive lenslet array (LA2).

The primary physical difference between the pixellated-mirror/lenslet array (LA1) and the second lenslet array (LA2) is illustrated in figure F2-5. Note that 4 columns of (pixellated) mirrors are interlaced between 4 columns of diffractive lenslets, while the entire LA2 is comprised of an 8 by 8 array of lenslets. As will be described below, the mirrors were used to route incoming beams from the previous stage toward the Hybrid/SEED SPA.

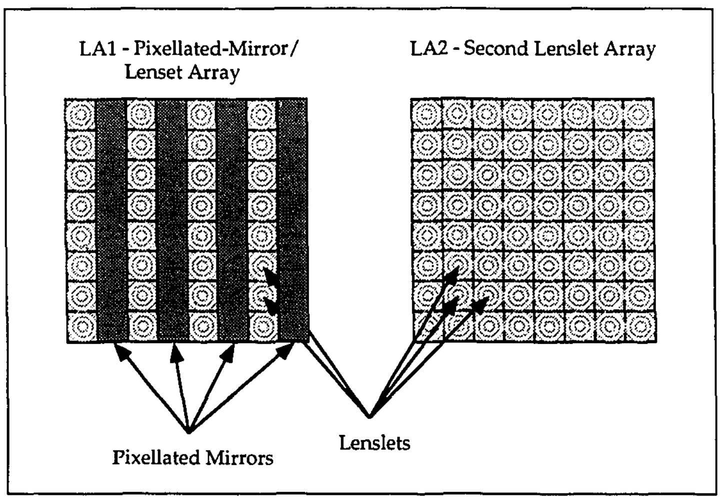

Figure F2-5: Schematic differences between the LA1 and LA2

The reflected (modulated) light off of the modulators on the Hybrid/ SEED chip was then re-collimated through the lenslet array (LA2), and its polarization linearized to s-polarization through QWP2. Entering the PBS, the s-polarized light then reflected off the PBS mirror, to be routed to the next stage.

Figure F2-4 also illustrates the light relayed from the previous stage. This incoming light, still s-polarized, was reflected off the PBS mirror surface toward LA1, after passing through the QWP1 which circularized its polarization. The beams then hit the pixellated mirrors on LA1, and bounced back toward the device array, passing through the same optical path as the light from the OPS (as described above). The relayed beams however were displaced (in the x direction) 125μm away from the OPS beams, thus impinging detectors (as opposed to modulators) on the Hybrid/SEED SPA.

It should be noted future reference that the QWP1, PBS, and QWP2 were pre-glued (by the supplier Meadowlark Optics) into what was collectively called the PBS-QWP assembly. The PBS-QWP assembly, LA1 and LA2 were mounted onto an optomechanical housing called the lenslet barrel, which, along with the OPS module resided within a larger housing called the outer barrel. A picture of the assembled system is shown below in figure F2-6.

Figure F2-6: Photograph of assembled system

2.2 Optical Power Supply Requirements

The optical and optomechanical requirements analysis of the system demonstrator directed a modularized approach to the design. The following subsections embody the results of this analysis pertaining to the OPS module to provide a full and comprehensive foundation for its design.

2.2.1 Optical Requirements of the Optical Power Supply

The 32 modulator windows (20μm by 20μm) on the device array (figure F2-1) represent the targets for the spot array having passed through the PBS-QWP assembly and the lenslets from the OPS (refer to figure F2-3). The requirements of the spot array at the output of the OPS, in order to hit the target modulators on the chip is given in Table T2-1, and a schematic of the desired spot array (looking in the direction of light propagation) is shown in figure F2-7. It should be noted that in the figure, the 8 by 4 central grid represent the signal spots (i.e. those impinging upon modulators on the device array), while the those on the periphery correspond to alignment spots used to facilitate the integration of the system demonstrator.

OPS Spot array requirement
8 by 4 focused spots on a uniform grid of 125μm (vertical) by 250 μm (horizontal)
8 additional peripheral spots
Spot array positioned between 18.34 ± 0.82mm away from the output of the OPS
$1/e^2$ irradiance spot radii of 6.47μm
Slower than f/6 beams generating spot array
Stable right-hand circularly polarized light
Minimal field curvature of spot array

Table T2-1: OPS Spot Array Requirements

OPS Spot array requirement
Power per spot greater than 250μW
Power uniformity across the entire array of greater than 90%.
Beam steering capabilities of better than: ± 400μm lateral translation ± 0.46° angular deviation
Spectral tolerance of 850±1nm

Table T2-1: OPS Spot Array Requirements

Although the requirements listed in Table T2-1 suffice for the Phase II system demonstrator, it was also desired that the optical design be flexible to accommodate a larger array of target modulators for scalability.

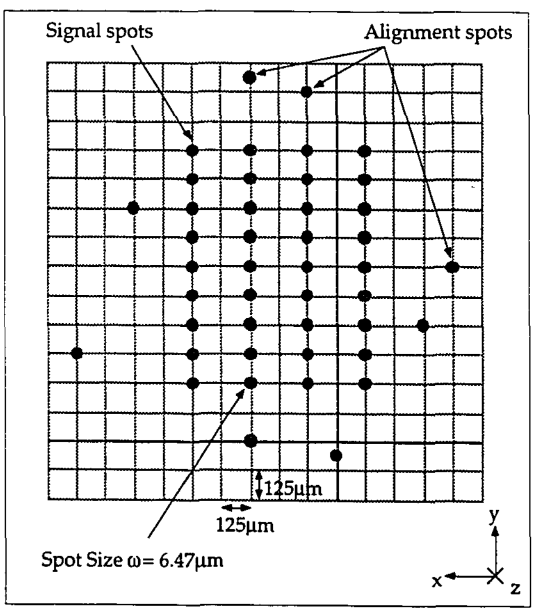

Figure F2-7: Schematic of the desired spot array at the output of the OPS

2.2.2 Optomechanical Requirements

The system demonstrator was built upon a vertically mounted baseplate housed in a standard 19" 6U VME commercial backplane chassis [4]. Based on the high level of integration, the optical power supply modules needed the following features:

- compactness
- robustness
- ease of machinability
- ease of assembly
- ease of alignment
- modularity

2.3 Summary

In order to facilitate the integration of the system, a modularized approach was adopted, such that each unit of the system could be pre-assembled and aligned. With this mind-set, the interconnection scheme for 4 optoelectronic Hybrid/SEED SPAs was envisaged employing a fairly complex optical interconnect, housed within a standard commercial backplane VME chassis. From this analysis emerged a set of well defined requirements for the OPS. In the following chapters, a dissection of the optical and optomechanical design of the OPS will be provided. Preceding which, however, a discussion of the light provision will be presented.

2.4 References

[1] D. V. Plant, B. Robertson, H. S. Hinton, M. H. Ayliffe, G. C. Boisset, D. J. Goodwill, D. N. Kabal, R. Iyer, Y. S. Liu, D. R. Rolston, W. M. Robertson, and M. R. Taghizadeh, "A multistage CMOS-SEED optical backplane demonstrator system," Opt. Comput. **96**, 14—15 (1996).

[2] ARPA/AT&T Hybrid SEED Workshop, July 18—21, 1995, George Mason University, Virginia (1995).

[3] D. R. Rolston, D. V. Plant, T. H. Szymanski, H. S. Hinton, W. S. Hsiao, M. H. Ayliffe, D. Kabal, M. B. Venditti, P. Desai, A. V. Krishnamoorthy, K. W. Goosen, J. A. Walker, B. Tseng, S. P. Hui, J. C. Cunningham, and W. Y. Jan, "A hybrid-SEED smart pixel array for a four-stage intelligent optical backplane demonstrator," IEEE Journal of Selected Topics in Quantum Electronics, **2**, 97—105 (1996).

[4] IEEE Standard 1014 for a Versatile Backplane Bus: VMEbus (1987).

CHAPTER 3 Light Distribution System

In order for the optical power supply to provide the desired output, it was imperative that the light provided at its input be extremely well behaved. A light distribution system was designed and characterized to provide the light to the system demonstrator. This chapter describes two methods that were attempted. The first using polarization maintaining fiber splitters, was rejected, and replaced with the second employing pellicles. A description of the light distribution systems are presented in section 3.1. Characterization results are presented in section 3.2.

3.1 Light Source Distribution System Description

As was shown in figure F2-3, the system was a four stage optical backplane, with each stage requiring an OPS to provide the array of constant optical power beams to illuminate the modulators on the respective Hybrid/SEED chip. For simplicity, optomechanical compactness, and ease of pre-alignment, light was launched into the OPS via a single mode polarization maintaining fiber. For practicality purposes, a single 500mW tunable laser with an external grating for wavelength selection and stabilization (Spectra Diode Labs Model # SDL 8630 Tunable Laser Diode System) was used to provide the light for all four stages (see figures F3-1 or F3-2). A 500mm focal length lens was used to squeeze the beam through the 4.8mm aperture of a Faraday isolator (OFR Part # IO-5-TIS2), and re-collimated to a ($1/e^2$ irradiance) beam diameter of 1.2mm through a 200mm lens. The Faraday isolator was used to eliminate backreflections into the laser, and a Glan Laser polarizer (OFR Part # PEH-8-TIS2) was used to improve the extinction ratio to better than 40dB (which was beyond the measurement capabilities of the Newport Model # 2832-c dual-channel power meter equipped with Model # 818-ST/ CM detector heads).

The first approach of light distribution employed the use of a tree of three 1:2 fiber splitters (JDS Fitel Part # AC-PM11-850-FP) as shown in figure F3-1. However, due to power loss and polarization instabilities, this arrangement was rejected.

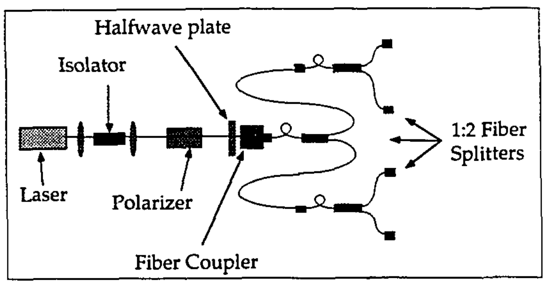

Figure F3-1: Light Distribution System Using Fiber Splitters

A second arrangement was employed using three thin membrane (linear-polarization preserving) pellicles (National Photocolor Order Spec: 1" Pellicle ETP Coated 50/50 for p-pol @850nm @45^{o}), as shown in figure F3-2, which incurred no significant power losses nor polarization instabilities. Characterization results will be provided in the next subsection for both of these systems.

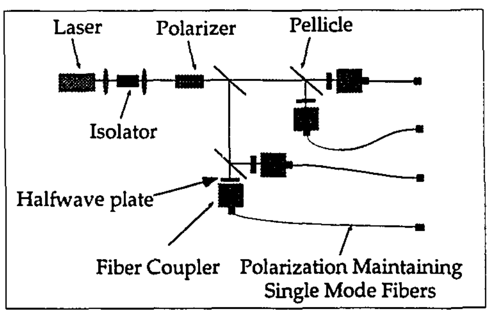

Figure F3-2: Light Distribution System Using Pellicles

In the pellicle arrangement, each beam was subsequently coupled into a 1 meter polarization maintaining (PM) single mode fiber (Fujikura PANDA^{tm} 850nm (see Note [A] in Appendix C) - supplied by JDS Fitel Part # A0101564) using a fiber coupler (Oz Optics Part # HPUC-23-850-P-6.2AS-11) to provide the optical inputs to each OPS module. Spectral stability was maintained by the laser to 850.0±0.05nm which was within the ±1nm spectral tolerance demanded by the SEEDs.

3.1.1 Optimally Launching Light into a Polarization Maintaining Fiber

Following the very simple alignment technique provided by the supplier of the fiber coupler (Oz Optics), 70% of the incoming light was launched into the fiber.

Aligning the linearly polarized light along the PM fiber's fast axis was experimentally verified to provide better polarization stability at the output compared to launching along its slow axis. The determination of this conclusion was dependent on the experimental method used to optimally align the polarization into the PM fiber.

Several methods of optimally orienting the polarization of the incoming light into a PM fiber have been reported [1][2]. These techniques being too time-inefficient and unnecessarily complicated were replaced with an extremely easy and quick method which produced excellent results.

The experimental setup is illustrated in figure F3-3. Two halfwave plates (HWP1 and HWP2), a collimating lens and a polarizing beamsplitter (PBS), in conjunction with a Newport dual-channel power meter (Model # 2832-c) were used to perform the alignment. By actively monitoring the real-time data acquisition (via a GPIB interface to a computer) of the ratio of the powers read from channels A and B of the meter, the optimal orientation of HWP1 was achieved by the following iterative method:

- Adjust HWP1
- Adjust HWP2 to maximize the ratio: $P_A/(P_A + P_B)$
- Repeat

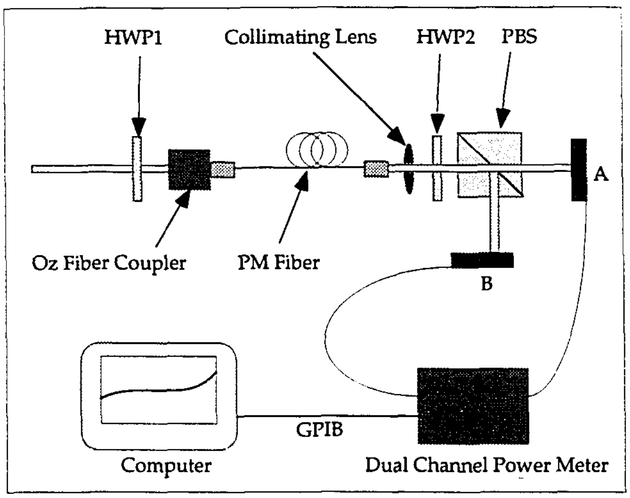

Figure F3-3: Experimental Setup to Orient the Polarization of the Light

Results showed that aligning the linear light along the PM fiber's slow axis resulted in variations of ±5% of the ratio $P_A/(P_A + P_B)$, while launching light along the fast axis resulted in only a ±0.05% variation (i.e. a negligible variation), indicating that the polarization stability of the light launched along the fast axis was far superior. For more information on PM fibers, the following references provide an excellent description: [3], [4].

The polarization extinction ratio of the light emitted from the fiber was then measured to be 28dB. Note that this was the linearity of the light entering each OPS.

3.2 Characterization of Light Distribution System

Measurements were performed on the laser, the fibers, the fiber splitters and pellicles. Analysis of these results stated that the fiber splitting arrangement was clearly not adequate for the application. However, with the implementation of the pellicle setup, it was shown that excellent performance was achieved. A final subsection on the characterization of the optical power budget of the pellicle system is also presented.

3.2.1 Laser Characterization

The characterized date for the SDL 8630 tunable laser diode system was given from the manufacturer (Spectra Diode Labs) as follows:

- 500mW@ 1.92 Amps (@21.0 °C maintained by a thermo-electric cooler)
- Diffraction limited, collimated beam
- 20nm tuning range (845 — 865 nm)
- Center wavelength 855nm
- <10GHz spectral width
- $M^2_{\perp} = 1.2$
- $M^2_{||} = 1.5$

The L-I (laser power vs. current) curve of the SDL 8630 was monitored periodically over the Phase II demonstrator implementation period. Graph G3-1 illustrates two interesting behavioral characteristics of the laser. First, the threshold current has been steadily increasing, indicating the aging of the chip. Chip degradation is however not apparent as the slope efficiency of the laser has not changed noticeably over time. It should be noted that the specified value for the threshold current is approximately 1.70Amps. Second, it was noted that upon laser start up, instabilities were present and manifest as jagged LI curves (the June 10, 96 - 'a' curve). However, after allowing the laser to relax into steady state operation for approximately 25 minutes, a second curve (the June 10, 96 - b curve) shows a smooth LI relationship.

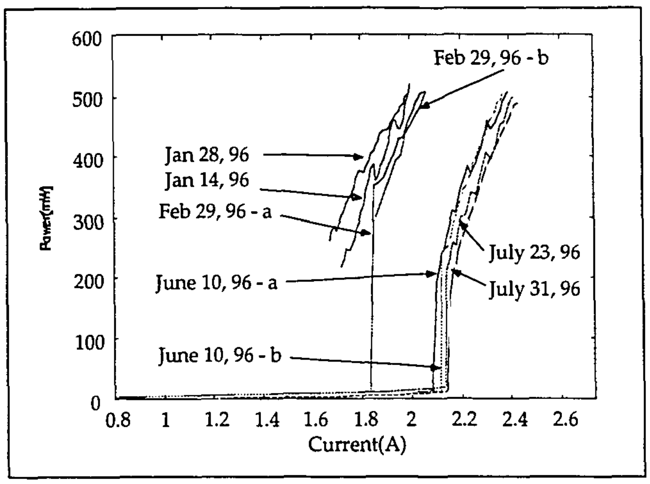

Graph G3-1: L-I Curves for the SDL 8630

Power stability measurements were conducted using a Newport 1835 single channel power meter (via a GPIB interface to computer). The results are displayed in Graph G3-2. The very interesting point of note is the power fluctuations over the first 50 minutes following laser start-up, caused by mode hopping and temperature instabilities. A second graph of measurements conducted after the laser had been operated for over one hour is presented in Graph G3-3. Based on this graph, the power fluctuation over time was measured to be 0.93% with respect to the mean.

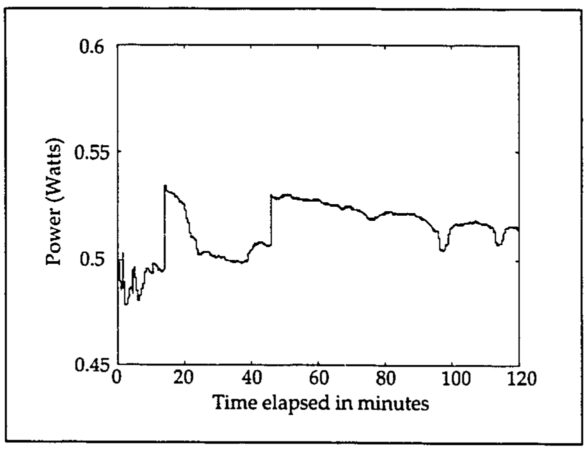

Graph G3-2: Power Stability Measurements of the SDL 8630 upon Start-Up

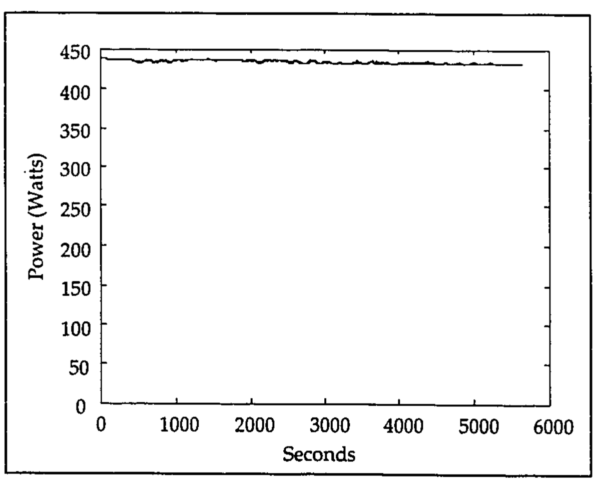

Graph G3-3: Power Stability Measurements of the SDL 8630 after 1 hour

It should be noted that the SDL 8630 was purchased in the fall of 1994. It was, at that time, released as a preliminary product with no long-term characterization specifications available. Thus the lifetime of the laser diode was unknown but estimated to be approximately 2000 hours (by the manufacturer). As of March 1997, it is estimated that over 1500 hours of use has been logged on the unit.

Although spectral behavioral characterization of the SDL 8630 has not been conducted over the span of the year, latest testing (as of February 1997) has shown that the spectral stability of the laser is very sensitive to thermal cycling. This is not unexpected, considering the lifetime of the laser [5].

The polarization extinction ratio at the output of the SDL 8630 was measured to be 20dB. The angular variations (i.e. polarization stability) of the polarization ellipse was negligible (beyond the capabilities of the measuring system).

3.2.2 Characterization of the Fibers and the Fiber Splitters

The extinction ratio of the light that was launched into the Oz Optics fiber couplers (after the Glan Laser polarizer) was measured to be better than 37dB. (Using a power meter and a Polarcor^{tm} polarizer (see Note [A] in Appendix C), it was difficult to obtain a more accurate reading).

With the introduction of the fiber splitters, it was measured that the total excess loss of each splitter (on average) was 22 ± 1%. Implementing the fiber tree using three fiber splitters, at the output of the tree a total excess loss of 39 ± 1% was measured. Thus only approximately 12 to 15mW will appear at the output of each output fiber of the tree with an input of 100mW.

The measured extinction ratio at the output of the fiber tree was measured only to be between 10dB and 20dB. (Note that input was better than 37dB). Also, by placing a QWP at the output of the output fiber, and observing the stability of the light passing through a QWP-PBS assembly, a thoughput oscillation of 7% was measured, indicating a large and unacceptable polarization instability.

3.2.3 Characterization of the Pellicles

Experimental characterization of the pellicles showed excellent polarization maintenance for p-polarized linear light. The extinction ratio of the light at the output of the Glan Laser polarizer was measured to be better than 37dB (as mentioned in the previous section). Measurements made at the output of the pellicles also resulted in figures of about 37dB or better, thus indicating that the pellicles did not effectively degrade the polarization extinction ratio.

After optimally launching light into a single PANDA^{tm} polarization maintaining (PM) fiber, it was measured that the power fluctuations at the output of the PM fiber was at worst-case ±0.22%, with an extinction ratio of 28dB.

3.2.4 Optical Power Budget for the Pellicle Light Distribution

The optical power budget (i.e. the optical loss characterization) for the pellicle based light source distribution system is given below in Table T3-1. The values that are presented are the measured throughput efficiencies with a precision of ±0.5%. It is seen that the excess loss (not including the splitting loss) from the laser source to the fiber coupler is 74.6% ±0.5%. It should also be noted that 2 additional components have been added (which do not appear in figure F3-2) to the optical train: namely the first halfwave plate and the PBS. These were added to split light off for other experiments. It is also shown that if 500mW is supplied by the laser, 65.3mW will be supplied at the input of each OPS. As will be discussed in Chapter 8, this was more than sufficient for the successful operation of the OPS, and the demonstrator as a whole.

Employing the excess loss numbers mentioned above for the fiber tree, it can be calculated that the pellicle arrangement was 36% more efficient than the fiber splitting setup.

Component	Transmission (%)	Cumulative Transmission (%)
500mm lens	99.2	99.2
OFR Faraday isolator	93.0	92.3
200mm lens	98.2	90.6
Halfwave plate	99.0	89.7
PBS	95.0	85.2
OFR Glan Laser polarizer	92.0	78.4
2 Pellicle splitting	25.0 (average)	19.6
2 Pellicles	96.0	18.8
Halfwave plate	99.2	18.7
Oz fiber coupler	70.0	13.1

Table T3-1: Optical Power Budget for the Pellicle Light Source Distribution System

3.3 Summary

Requirements of the OPS listed in Chapter 2 state that light of small spectral linewidth, enough power, and stable polarization be supplied at the input of each OPS module. By implementing a fiber-splitting arrangement, it was experimentally verified that both the power loss, as well as the polarization instabilities incurred were unacceptable. Thus a second arrangement employing the use of thin membrane pellicles was adopted, resulting in a much higher throughput efficiency, and excellent polarization stability.

3.4 References

[1] G. R. Walker, N. G. Walker, "Alignment of Polarisation-Maintaining Fibres by Temperature Modulation", Electronics Letters, **23,** 689—691, (1987).

[2] N. Caponio, C. Svelto, "A Simple Angular Alignment Technique for a Polarization-Maintaining-Fiber", IEEE Photonics Technology Letters, **6,** 728—729, (1994).

[3] J. Noda, K. Okamoto, Y. Sasaki, "Polarization Maintaining fibers and their applications", Journal of Lightwave Technology, **LT-4,** 1071—1089, (1986).

[4] F. M. Sears, "Polarization maintenance limits in polarization maintaining fibers", Journal of Lightwave Technology, **8,** 684—690, (1990).

[5] Laser Diode Operator's Manual & Technical Notes, Spectra Diode Labs, 1994.

CHAPTER 4 Optical Design

The design of the OPS can be thought of as being split into two separate parts: the optical design and the optomechanical design. These parts are very highly coupled, and require a parallel engineering effort to succeed. In order to facilitate the presentation, the issues pertaining to the optical design of the OPS are presented in this chapter, while those pertaining to the optomechanical design are presented in the following. The optical design of the OPS is presented in section 4.1, with mathematical explanations of the models used. The heart of the OPS was the multiple phase grating, and a full description of its design and functionality is presented in section 4.2. A third section elaborating on the design simulation results appears in section 4.3, followed by an analysis of the optical power budget in section 4.4.

4.1 Optical Power Supply Optical Design

The optics were designed to meet all the spot array requirements while reducing the optomechanical complexities to a minimum. A schematic of the optical design is shown in figure F4-1 with the nominal values of element separation.

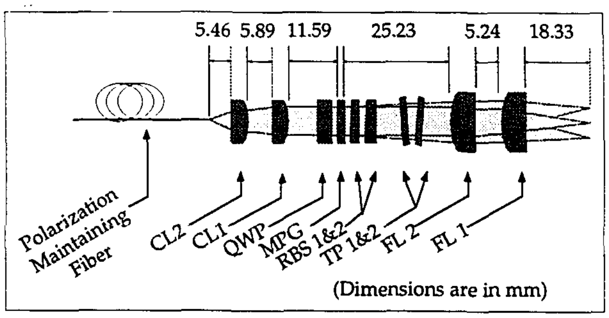

Figure F4-1: Optical Design of the Optical Power Supply

Perfectly linearly-polarized light was assumed to be emitted from the single mode polarization maintaining (PM) fiber placed at the front focal plane of the compound collimating lens (CL1, CL2). The mode field diameter ($1/e^2$ irradiance) of the fiber was specified to be 5.6μm. The collimated beam diameter at the output of the collimating lens was designed to be 2.30mm. After passing through the zero-order quarterwave plate (QWP) to right-hand circularize its polarization, the beam was then passed through the MPG. The angularly diffracted collimated beams then propagated through the Risley beam steerers (RBS 1 & 2) and tilt plates (TP 1 & 2) until they were focused by the compound Fourier lens (FL 1, FL 2) to spots in the Fourier plane of ($1/e^2$ irradiance) radii of 6.47μm.

Based on the nominal numbers used in the optical design, the speed (f/#) of the focused beams at the output of the OPS was f/12.07 ($1/e^2$ irradiance diameter of 2.30mm). This was well within the f/6 limit demanded by the lenslets.

A Gaussian beam propagation model was the starting point for the optical design. The following subsection presents the mathematical foundations of such an analysis, and its context within the optical design of the OPS. A subsequent subsection on the use of two-element compound lenses for adjustment of focal length is then given, followed by the final subsection on the optical and optomechanical degrees of freedom of the OPS.

4.1.1 Gaussian Beam Propagation Model

The following presentation assumes that the reader is familiar with basic electro-magnetic theory, especially Maxwell's equations. The motivation for this analysis is to derive a relationship between a (Gaussian) beam's radius as a function of axial distance, since the beam emitted from a fiber has been mathematically and experimentally verified [1 - Ch.7] to approximate a Gaussian beam very closely. The transformation of a Gaussian beam through a lens is also derived, in order to be able to determine its propagation through the OPS.

The starting point of Gaussian beam propagation analysis begins with representing the wave which is under scrutiny as a paraxial wave (i.e. its wavefront normals are paraxial rays) [1 - Ch.2]. Thus the paraxial wave $U(\bar{r})$ (where $\bar{r} = (x, y, z)$ can be described by a plane wave $\exp(-jkz)$, propagating in the positive z axis (where $j=(-1)^{0.5}$, and k is the propagation constant equalling $2\pi/\lambda$), with a slowly varying complex amplitude (along the z direction with respect to the wavelength) $A(\bar{r})$:

$$U(\bar{r}) = A(\bar{r})\exp(-jkz) \ . \tag{1}$$

Applying paraxial approximations to the Helmholtz equation:

$$\nabla^2 U(\bar{r}) + k^2 U(\bar{r}) = 0 \tag{2}$$

results in the paraxial Helmholtz equation:

$$\nabla_T^2 A \ - \left(j2k \cdot \frac{\partial}{\partial z}(A)\right) = 0 \ , \tag{3}$$

where the Laplacian operator (with the subscript T) is the transverse Laplacian operator:

$$\nabla_T^2 \ = \frac{d^2}{dx^2} + \frac{d^2}{dy^2} . \tag{4}$$

The simplest solution of the paraxial Helmholtz equation (equation 3) is the paraboloidal wave [1 - Ch.3]:

$$A(\bar{r}) = \frac{A_1}{z} \cdot \exp\left(-jk\frac{\rho^2}{2z}\right) \text{, where } \rho = x^2 + y^2 \text{ and } A_1 \text{ is a constant.} \tag{5}$$

Another solution to the paraxial Helmholtz equation is the Gaussian beam. By substituting a translational shift transformation, $q(z) = z - \xi$, where ξ is a purely imaginary constant ($-jz_o$, and z_o is real), the solution to equation 3 becomes:

$$A(\bar{r}) = \frac{A_1}{q(z)} \cdot \exp\left(-jk\frac{\rho^2}{2q(z)}\right) \ . \tag{6}$$

Separating $1/q(z)$ into its real and imaginary parts, and defining $R(z)$ and $\omega(z)$ to be measures of the radius of curvature and beam radius respectively, results in:

$$\frac{1}{q(z)} = \frac{1}{z + jz_o} = \frac{1}{R(z)} - j\frac{\lambda}{\pi \cdot \omega^2(z)}. \tag{7}$$

Substituting equation (6) and equation (7) into equation (1), results in an expression for the complex amplitude $U(\bar{r})$ of the Gaussian beam:

$$U(\bar{r}) = A_o \cdot \frac{\omega_o}{\omega(z)} \cdot \exp\left(\frac{-\rho^2}{\omega^2(z)}\right) \cdot \exp\left(-jkz - jk\frac{\rho^2}{2R(z)} + j\zeta(z)\right) \tag{8}$$

where $(A_o = A_1/jz_o)$ and:

$$\omega(z) = \omega_o\left(1 + \left(\frac{z}{z_o}\right)^2\right)^{\frac{1}{2}} \tag{9}$$

$$R(z) = z\left(1 + \left(\frac{z_o}{z}\right)^2\right) \tag{10}$$

$$\zeta(z) = \operatorname{atan}\left(\frac{z}{z_o}\right) \tag{11}$$

$$\omega_o = \left(\frac{\lambda z_o}{\pi}\right)^{\frac{1}{2}} \tag{12}$$

where ω_o represents the beam waist radius and z_o represents the Raleigh range (measure of the depth of focus, i.e. depth of focus = $2z_o$). These formulas (9 - 12) represent the set of formulas relevant for modeling Gaussian beams.

Transmission of a Gaussian beam through a thin lens results in a multiplication of the complex amplitude transmittance of the lens: $\exp(jk\rho^2/2f)$ [1 - Ch. 2] by the complex amplitude of the beam (equation 8), resulting in another Gaussian beam with a different radius of curvature and beam waist. This is illustrated in figure F4-2 below.

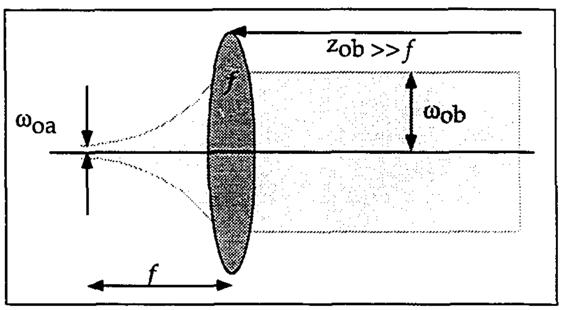

Figure F4-2: Gaussian Beam Through a Lens

Assuming that the (small) incoming beam waist is located at the front focus of the lens (as shown in the figure), the resulting output beam waist of the transmitted beam (if the output Raleigh range z_{ob} is large in comparison to the focal length f of the lens) is approximated by the following relationship:

$$\omega_{ob} = \frac{f \cdot \lambda}{\pi \cdot \omega_{oa}}. \tag{13}$$

For details on the derivation of this approximation, the reader is referred to [1 - Ch.3]. Note that since the property of light is reversible, the light could just as easily be travelling right to left in figure F4-2.

In the context of the OPS design, there were effectively two lens transformations occurring: (i) the collimation of the beam emitted from the fiber, and (ii) the focusing of the collimated beam at the output of the OPS. Labelling the beam waist radius at the fiber facet as $\omega_{o\text{-}f}$, the collimated beam radius through the OPS as ω_{mpg}, and the beam waist radius of the focussed beam at the output of the OPS as $\omega_{o\text{-}spot}$, the following relationships result, after utilization of equation 13 twice:

$$\omega_{o-spot} = (\omega_{o-f}) \cdot \frac{f_f}{f_c} \tag{14}$$

where f_f and f_c are the focal lengths of the Fourier and collimating compound lenses respectively. It is interesting to note that the ω_{mpg} does not appear in the relationship. It should be noted that the Raleigh range of the collimated beam is approximately 4.9 meters, which is much larger than both the effective focal distances of the compound collimating and Fourier lenses (as will be given in the next subsection), and therefore the use of equation 13 to derive equation 14 is justified. More information about compound lenses and their effective focal lengths is given in the next subsection.

4.1.2 Two-Element Compound Lenses

Two-element compound lenses with variable focal lengths were chosen for both the Fourier lens and the collimating lens to account for uncertainties in the mode field diameter of the input fiber, the lens focal length specifications, and aberrations of the beams through the OPS. The lenses were oriented in the Petzval configuration [2] which provided the best performance in terms of aberrations, flexibility, optical power division, size, and cost. A more detailed explanation of the variability of the focal length is provided in the next subsection.

In the Petzval configuration, the optical power is split equally between the two parts of each compound lens. Hence the aberration is minimized, and the focal length of the lens is easy to adjust with high resolution by altering the air gap. Although a Plossl configuration is similar and has been used in another free-space optical system [3], simulations showed that in our application, the Petzval configuration gave lower aberrations for each spot. A Cooke's triplet, which has been used in an earlier modulator array application [4][5], was another option for the Fourier lens due to its exceptionally flat field. However, commercial Cooke's triplets have their focal length specified to only ±1%, compared to 0.4% required for the OPS optical design to define the correct spot separation. Since the optical power in a Cooke's triplet is divided very unequally across the three elements, adjusting the focal length requires extremely fine changes to the element spacings.

At their nominal (Petzval configuration) positions, the compound collimating lens had a focal length of 12.90mm, and the compound Fourier lens had a focal length of 27.78mm. Achromat doublets were used for all lenses due to their minimal spherical aberration, minimal wavefront distortion, and tight focal length tolerance.

It should be noted that although a true Fourier lens should introduce $f \cdot \sin\theta$ distortion, at the maximum diffracted angle designed to be 0.0068^{o} within the OPS, the small angle approximations hold. Therefore, an off-the-shelf lens pair was used due to cost and convenience. A more detailed explanation of the Fourier lens distortion will be provided in the following section on the Multiple Phase Grating.

4.1.2.1 Variability of Focal Length With a Thick Compound Lens

It is assumed that the reader is familiar with thin lens paraxial optics in the following presentation.

Figure F4-3 illustrates a single thick lens of thickness 't', and some points of interest: namely its vertices, V_1 and V_2, its principal points H_1 and H_2, and its focal points F_1 and F_2. The vertices are the points at which the optical axis intersects the lens' front and back surfaces. The principal points define the intersection of the principal planes with the optical axis, where the principal planes (using the paraxial optical limit) is defined to be the locus of the (extended) collimated rays intersecting a corresponding (extended) focused ray propagating to its nearest focal point. The front focal length (*ffl*) and the back focal length (*bfl*) are the respective distances measured from the foci to its nearest vertex [6][7].

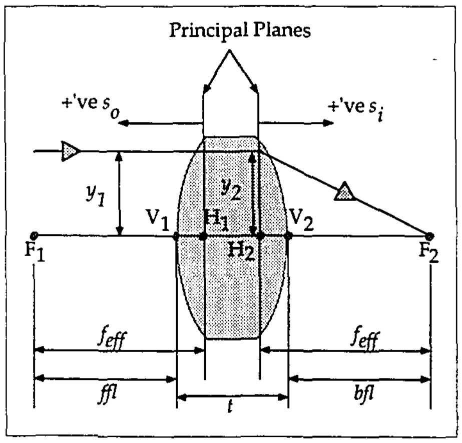

Figure F4-3: A Thick Lens

With this set of nomenclature, one is now able to define the expression for conjugate points (in the Gaussian form):

$$\frac{1}{s_o}+\frac{1}{s_i} = \frac{1}{f_e} \tag{15}$$

where f_e is the effective focal length of the thick lens, provided that s_o and s_i are measured from the first and second principal planes respectively (and that s_o is positive when the object is to the left of H_1 while s_i is positive when the image is to the right of H_2. Note that this is the same formula for the thin lenses. A very important result emerges from a more detailed analysis: namely, all thin lens formulas hold when the measurements are made from the principal planes [6][7].

The principal points are therefore conjugate with one another, and any ray directed to a point on one principal plane at height y_1 will appear to have emerged from the lens from a point on the second principal plane at height $y_2 = y_1$.

Arranging two thick lenses in a compound arrangement as shown in figure F4-4 separated by a distance *'d'* measured from the two closest principal planes (namely H_{12} and H_{21}) (where the first subscript denotes the respective lens), a new pair of effective principal planes is created, called H_1 and H_2 (Note that in the figure, only the second effective principal plane is shown). An expression for the effective focal length of the lens system results:

$$f_{eff} = \frac{f_1 \cdot f_2}{f_1+f_2-d}. \tag{16}$$

Note that *'d'* is not truly the lens separation. In fact, the lens separation *'s'* is directly related to *'d'* after subtracting the vertex - to - principal plane distances:

$$s = d-\overline{H_{12}V_{12}}-\overline{H_{21}V_{21}} \quad . \tag{17}$$

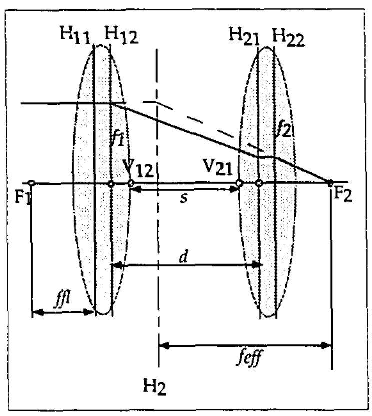

Figure F4-4: Compound Two-Element Thick Lens

Thus it has been shown that a change of the lens separation results in a change in the compound lens system's effective focal length. Plotted in Graph G4-1 is the relationship between the effective focal length to lens separation, given the nominal values for the design of the collimating lens for the OPS, namely $f_1 = f_2 =$ 20mm, and ranging '*d*' between 5 and 11 mm (note that the nominal spacing '*s*' between the lens as per the optical design is 5.46mm, which corresponds to a *d* of 8.08mm using the supplier's values for the vertex to principal plane distances).

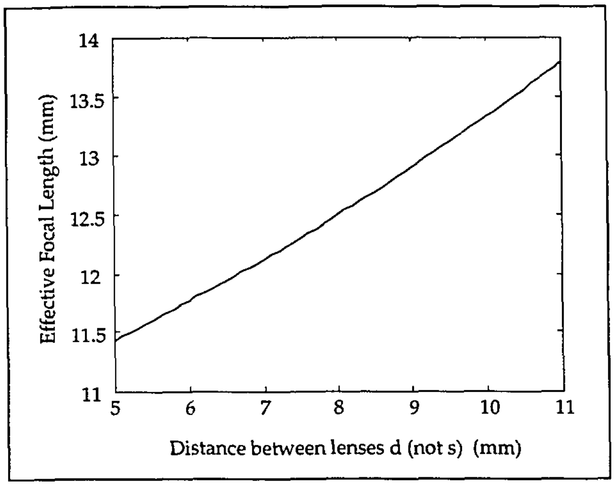

Graph G4-1: Effective Focal Length versus Distance between Lenses

The *ffl* of the compound lens is described by:

$$ffl = \overline{F_1 H_{11}} = \frac{f_1 \cdot (d - f_2)}{d - (f_1 + f_2)} \qquad (18)$$

where the *ffl* is measured from the front focal point to the first principal plane of the first lens.

The relationship between the *ffl* and the lens separation '*d*' ranging from 5mm to 11mm with two 20mm lenses is presented in Graph G4-2. From analysis of Graph G4-1 and Graph G4-2, it is clear that for a given lens separation, there is a unique position of the compound lens (i.e. the lens pair) with respect to a fixed point; in context with the OPS, that fixed point being the fiber facet. A schematic of the resulting arrangements for three different lens separations is shown in figure F4-5. This figure also illustrates the relationship with the output beam diameter to the effective focal length of the lens pair (see equation 13). This relationship was critical in the alignment of the collimating lenses, and will be described more fully in Chapter 6.

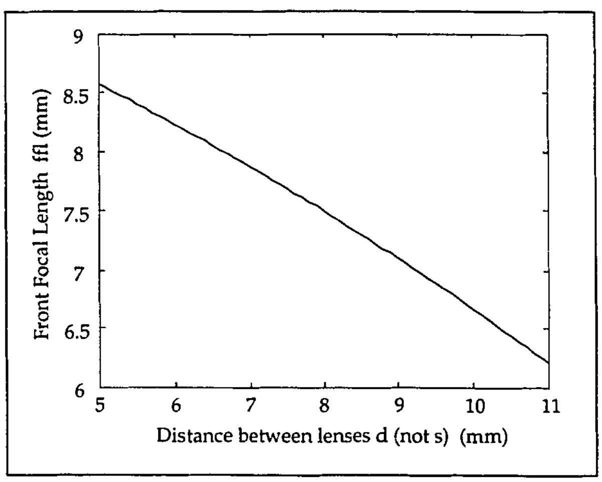

Graph G4-2: Front Focal Distance versus Distance between Lenses

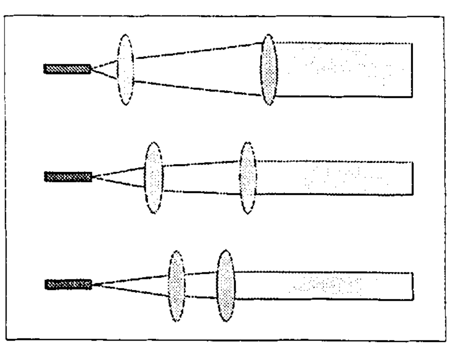

Figure F4-5: FFL versus Effective Focal Length and Output Beam Diameter

4.1.3 Optical and Optomechanical Degrees of Freedom

The OPS design had a number of optical and mechanical degrees-of-freedom in order to meet the set of design requirements; these are presented in Table T4-1.

By analysis of these optical and optomechanical degrees-of-freedom, as well as the OPS module requirements listed in Chapter 2, a barrel design was chosen to house the elements of the OPS. More information about the optomechanical design will be presented in Chapter 5.

Detailed Design Requirement	Optical/Optomechanical Solution
Spots on a uniform grid	Chose a low distortion Fourier lens
Spot separation matched SEED separation	Adjusted focal length of Fourier lens by changing element separation
$1/e^2$ irradiance spot size of 6.47μm	Adjusted focal length of collimating lens by changing element separation
Collimated beam through the planar elements	Maintained the fiber facet at the front focus of the collimating lens
Wavefront flatness of less than $\lambda/20$	Chose a low aberration Fourier lens; Aberrations from other elements kept low; Maintained fiber at front focus of collimating lens
Angular alignment of spot array about optical axis	Rotated MPG about optical axis
Pitch and yaw alignment of spot array with respect to interconnect	Adjusted the difference in the roll position of the opposed tilt plates
Mutual angular alignment of chief rays of all beams in the spot array	Positioned MPG at front focus of Fourier lens; Chose low distortion Fourier lens
Lateral alignment of spot array	Rotated the Risley prisms about the optical axis

Table T4-1: Optical and Optomechanical Degrees of Freedom

4.2 Multiple Level Phase Grating Design

The fundamental challenge in designing the OPS was in the generation of the array of 8 by 4 (+ 8 alignment) spots such that the 6.47μm ($1/e^2$ irradiance) radii spots were accurately positioned across the 125μm grid with uniform power distribution. There exist numerous techniques for producing spot arrays from a single beam [8][9]. Our system employed Fourier-plane array generation, utilizing a computer generated hologram implemented as a multiple level phase grating (MPG).

The MPG was designed using a simulated annealing algorithm [9][10] to create a grating composed of a periodic array of unit cells that could generate the desired spot array in the focal plane of a Fourier transform lens; the grating itself representing the 2-dimensional spatial inverse Fourier transform of the spot array and placed at the front focal plane of the Fourier lens.

As shown in figure F4-6 below, a collimated beam will be diffracted through a grating at discrete angles described by the following relationship (where *n* is an integer and corresponds to the diffraction order):

$$P \cdot \sin(\theta) = m\lambda \tag{19}$$

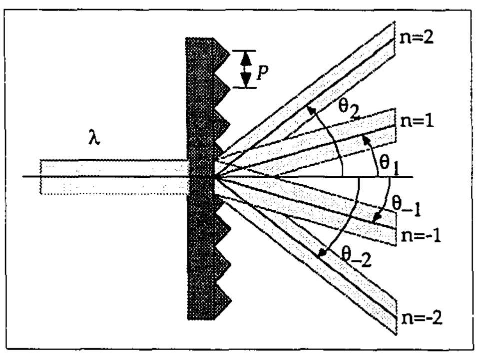

Figure F4-6: Collimated Beam Diffracted through a Grating

By placing the grating (MPG) at the front focal plane of the Fourier lens, the periodicity, P, of the grating is related to the spot spacing, S, in the Fourier plane (i.e. the output focal plane of the Fourier lens), by the relation given in equation 20, where λ is the wavelength and f is the focal length of the Fourier lens. It should be noted that this relationship results if the Fourier lens introduces an $f \bullet \sin(\theta)$ distortion of the spots at its output focal plane. The factor 2 in the formula arises because only even order spots were used in the grating design.

$$P = \frac{2 \cdot f \cdot \lambda}{S}. \tag{20}$$

For the system demonstrator requiring a spot spacing of S=125μm (on the smallest grid as was shown in figure F2-7) for the array of 8 by 4 spots, and based on the chosen optical design, each unit cell had a periodicity of P = 377.8μm by 377.8μm, divided into 128 by 128 pixels as shown in figure F4-7. Each square pixel had a dimension of $P/128$ = 2.95μm by 2.95μm, and had a height quantized to one of 8 levels; this is illustrated in figure F4-7. The MPG was made from fused silica and was not anti-reflection coated due to time constraints.

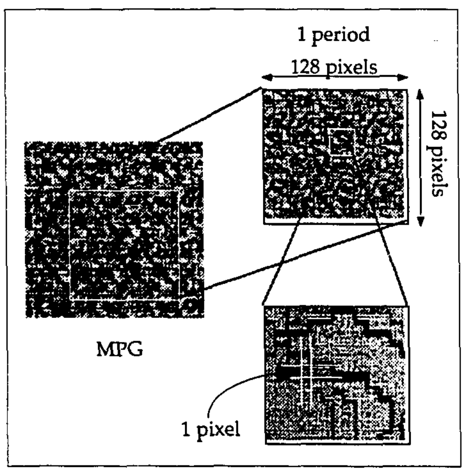

Figure F4-7: 8 Level Multiple Phase Grating

From the design program, the theoretical diffraction efficiency of the 8 level phase grating was predicted to be 83% (76.5% after the 4% reflections at each non-AR coated surface). The overall uniformity of the spots was predicted to be 96.9%, defined using the metric:

$$Uniformity = 1-\frac{(P_{max}-P_{ave})}{P_{ave}} = 1-\frac{(P_{ave}-P_{min})}{P_{ave}} = 1-\frac{(P_{max}-P_{min})}{P_{max}+P_{min}} \qquad (21)$$

where $P_{ave}=(P_{max}+P_{min})/2$.

Defining the collimated beam radius ($1/e^2$ irradiance) passing through the MPG to be ω_{bpg}, the number of MPG periods sampled, *NPS*, is defined to be:

$$NPS = \frac{2\omega_{bpg}}{P}. \qquad (22)$$

Also, from Gaussian beam propagation models (as will be explained in detail in subsection 4.1.1), the focused spot radius, ω_f, is related to the collimated beam diameter by:

$$\omega_f = \frac{f\cdot\lambda}{\pi\cdot\omega_{bpg}} \qquad (23)$$

where f is the focal distance of the Fourier lens, and λ is the wavelength.

The (linear) compression ratio, *CR*, can be defined as the ratio of the spot separation to the 99% spot diameter:

$$CR = \frac{S}{3\omega_f}. \qquad (24)$$

Thus, substituting equations 20, 22, and 23 into equation 24, a relationship between the compression ratio and the number of periods sampled is derived to be:

$$CR = \frac{\pi}{3}NPS. \qquad (25)$$

The number of periods sampled was NPS=6.1, where ω_{bpg} was designed to be 1.15mm, yielding a compression ratio of 6.37 through the relation given in equation 25 [11]. This value is sufficiently larger than the minimum CR_{min} of 3 which is required to ensure that the power uniformity is not degraded by aliasing [12].

The issue of scalability (which was introduced in section 2.2.1) was addressed by ensuring that a spot array of 16 by 8 spots at one-half the spot spacing (i.e. S=62.5μm to maintain the same field of view) be implemented by replacement of the MPG element alone, with no other modifications to the optical design. Based on this requirement, the period P of the MPG would be doubled, thereby reducing the NPS to a value of 3.05. This results in a CR of 3.19, which is still larger than the CR_{min} of 3.

4.3 Design Tolerancing, Modeling and Simulation

The total estimated lateral error of the position of the spot array with respect to LA1 (figure F2-4) was ±400μm. This value was calculated from the worst-case estimate of the fiber centering within the OPS barrel of ±100μm, which results in a ±230μm error of the spot array at the output of the OPS. As well, due to the accuracy to which the OPS barrel could be inserted in the outer barrel with respect to the LA1, machining tolerances, and centering of the lenses, an additional ±170μm lateral positioning error results. Thus a ±400μm error corresponds to a 0.54° minimum required wedge angle for the Risley prisms (SF10 glass). Wedge angles of 1° were chosen due to availability and cost.

Angular misalignment of the fiber input was estimated to be 1° in the worst case yielding a 0.46° angular deviation from the optical axis of the chief rays of the output spots. To compensate for this misalignment, a 3mm thick tilt plate (SF10 glass) oriented at 10.4° with respect to the optical axis was required. Traditional tilt plate design requires one parallel planar optical element to have rotational degrees-of-freedom along the two axes perpendicular to the optical axis (pitch and yaw). This approach was not well-suited for the barrel housing chosen for the OPS, which only conveniently provides optomechanical degrees-of-freedom in translation along, and rotation about the optical axis (roll). Therefore a novel two-element tilt plate design was implemented that requires only one degree-of-freedom, namely roll. Angular coverage of the spot array across the Fourier plane was achieved by permanently mounting two 1.5mm thick tilt plates (SF10 glass) at a fixed angle of 10^{0} (from the optical axis), and by appropriately positioning both elements in roll.

Gaussian beam power clipping due to the square apertures of the system (lenslets and modulator windows) of 0.54% was taken into account in the optical design. A full analysis of beam propagation through the optical interconnect showed that a 1% clipping effect is tolerable as long as the spot size is kept within tight tolerances.

The system was modeled using OSLO-Pro. Distortion of the spot array from the correct grid, field curvature, spot size variation, Strehl ratio, 1/RMS OPD, and the variations of the chief ray angles were calculated. The spot size was estimated in OSLO-Pro as the point spread function at the plane of best focus (minimum RMS OPD). In the point spread function calculation, a Gaussian apodization was applied at the first surface of the collimating lens. The width of this Gaussian function was given by a paraxial Gaussian calculation starting from a waist at the fiber facet. The OLSO design specifications is given in Appendix A.

Based on lateral adjustment provided by the Risley prisms, the simulation was carried out taking into account a maximum lateral displacement of the spot array of 575μm. Table T4-2 shows a summary of results of the simulation using the nominal design parameters as shown in figure F4-1. For each simulation, the calculated number for a spot located directly on the optical axis, for a corner signal spot of an on-axis spot array, and for a spot located 1152μm away from the optical axis (representing the outer corner spot of a 575μm diagonally shifted spot array) is given, along with the allowable tolerance values (shaded for clarity) based on 1% clipping of the beams by the modulator windows (on the Hybrid/SEED chip as shown in figure F2-1). Note that the tolerances for the minimum Strehl ratio and wavefront 1/RMS variation (1/RMS OPD) were set at 0.8 and 14 respectively [13, p 271][14].

Simulation	Tolerance for 1% clipping	On-axis spot	Corner spot of an on-axis spot array	Spot 1152μm off-axis
Distortion	±2.5μm	0μm	0μm	1.03μm
Field curvature	±63μm	0μm	11.5μm	46μm
Spot size	±0.25μm	6.47μm	6.50μm	6.75μm
Chief ray angle	±0.7°	0°	0.0008°	0.0068°
Strehl ratio	0.8	0.865	0.857	0.817
1/RMS OPD	14	43.2	43.5	28.9

Table T4-2: Simulation results and tolerance values

It is shown in the table that all simulation results (but one), for distortion, field curvature, spot size, chief ray angle, Strehl ratio, and wavefront 1/RMS variation fall within the tolerance limits for clipping of 1%. (Note that both the wavefront 1/RMS variation and Strehl ratio tolerances represent the minimum acceptable value). The spot size for the 1152μm diagonally shifted spot shows a simulation result of 6.75μm, which is 0.03μm larger than the maximum tolerance. As will be shown in Chapters 5 and 7, it was not necessary to displace the spot array this far, and was thus an acceptable result.

Note that the ±2.5μm distortion tolerance represents the maximum diagonal distortion for the corner spots. This corresponds to a tolerance on the spot separation of 125.00 ± 0.57μm which can be derived from an analysis of two distorted spots on the same side of the spot array, as shown in figure F4-8 below.

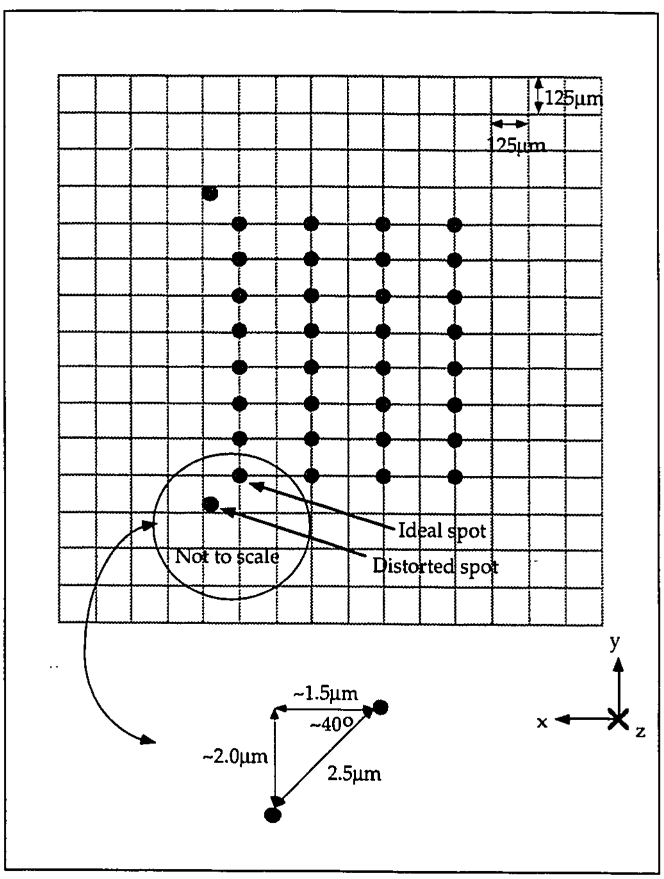

125μm
125μm
Ideal spot
Distorted spot
Not to scale
~1.5μm
~40°
~2.0μm
2.5μm
y
x
z

Figure F4-8:

4.4 Optical Power Budget

Table T4-3 shows the estimated impact that each component had on the overall throughput efficiency of the OPS. The values used in this budget were obtained from manufacturer's specifications. For convenience, the manufacturers and part numbers are provided in this table. The table shows that the total excess losses (not including fan-out losses) were estimated to be 100% - 71.4% = 28.6%; while the losses not including the MPG were estimated to be only 2.9%.

Component	Estimated throughput efficiency	Cumulative throughput efficiency	Manufacturer	Part #
Collimating lens 1	99.6%	99.6%	Spindler & Hoyer	32-2201
Collimating lens 2	99.6%	99.2%	Spindler & Hoyer	32-2201
Quarterwave plate	96.8%	96.0%	Meadowlark	NRQ-050-850
MPG	76.5%	73.5%	ARPA/CO-OP/ Honeywell Workshop	custom-made
Risley prism 1	99.5%	73.1%	Planar Optics	custom-made
Risley prism 2	99.5%	72.7%	Planar Optics	custom-made
Tilt plate 1	99.5%	72.4%	Planar Optics	custom-made
Tilt plate 2	99.5%	72.0%	Planar Optics	custom-made
Fourier lens 1	99.6%	71.7%	Spindler & Hoyer	32-2265
Fourier lens 2	99.6%	71.4%	Spindler & Hoyer	32-2265

Table T4-3: Optical power budget

4.5 Summary

The optical design herein presented was simultaneously done in conjunction with the optical and optomechanical design of the whole system demonstrator. However, it was possible to do much of the detailed design, modeling and simulation separately based on the list of well defined requirements as listed in Chapter 2. The heart of the OPS, namely the MPG was designed by Dr. William M. Robertson and manufactured through the ARPA/CO-OP/Honeywell DOE Workshop. After a detailed design and simulation of the optical performance of the system, the design of the optomechanics were then finalized. The details of the optomechanical design appears in the next chapter, and will serve to house the concepts presented in this chapter into a realizable module.

4.6 References

[1] B. E. A. Saleh, M. C. Teich, Fundamentals of Photonics, Wiley & Sons, Inc., New York (1991).

[2] R.E. Fischer and W.J. Smith, "Modern Lens Design - A Resource Manual", McGraw-Hill, pp. 221—238 (1992).

[3] F. B. McCormick, F. A. P. Tooley, T. J. Cloonan, J. L. Brubaker, A. L. Lentine, R. L. Morrison, S. J. Hinterlong, M. J. Herron, S. L. Walker, and J. M. Sasian, "Experimental investigation of a free-space optical switching network by using symmetric self-electro-optic-effect devices," Appl. Opt., **31**, 5431—5446 (1992).

[4] A. C. Walker, I. R. Redmond, D. J. McKnight, R. G. A. Craig, G. S. Buller, P. Meredith, M. R. Taghizadeh, "Construction of an optical cellular logic image processor", SPIE Proceedings, **1806**, 373—377, "1992 ICO Topical meeting on optical computing," Minsk, Byelorussia (1992).

[5] R. G. A. Craig, B. S. Wherrett, A. C. Walker, D. J. McKnight, I. R. Redmond, J. F. Snowdon, G. S. Buller, E. J. Restall, R. A. Wilson, S. Wakelin, N. McArdle, P. Meredith, J. M. Miller, M. R. Taghizadeh, G. Mackinnon, S. D. Smith, "First programmable digital optical processor: optical cellular logic image processor", SPIE Proceedings, **1505**, 76—78, "Optics for computer: Architectures and technologies", The Hague, Netherlands (1991).

[6] E. Hecht, "Optics", 2nd Ed., Addison Wesley, 1990.

[7] J. R. Meyer-Ardent, "Introduction to Classical and Modern Optics", 4th Ed., Prentice Hall, New Jersey, 1995.

[8] N. Streibl, "Beam shaping with optical array generators", Journal of Modern Optics, **36**, 1559—1573, (1989).

[9] M.P. Dames, R. P. Dowling, P. McKee, and D. Wood, "Efficient optical elements to generate intensity weighted spot arrays: design and fabrication", Appl. Opt., **30**, 2685—2691 (1991).

[10] A. G. Kirk, and T. J. Hall, "Design of binary computer generated holograms by simulated annealing: coding density and reconstruction error," Optics Communications, **94**, 491—496 (1992).

[11] Y.S. Liu, B. Robertson, D. V. Plant, H. S. Hinton, W. M. Robertson, "Design and Characterization of a microchannel optical interconnect for optical backplanes", accepted at Appl. Opt. (1996).

[12] F. B. McCormick, Photonics in Switching, edited by J. E. Midwinter, Academic Press, 1993.

[13] H. S. Hinton, An Introduction to Photonic Switching Fabrics, Plennum Press, NY (1993).

[14] J. E. Midwinter, Photonics in switching, Academic Press, pp.200 (1993).

CHAPTER 5 Optomechanical Design

Assembly of the components in the OPS required an elegant optomechanical design in order to produce a modular, compact & robust package. Given the optical design and the high level of integration of the system demonstrator, it was necessary to mount the optics in custom-made cells, and place these cells within a larger housing. Optimally, the method used to implement the housing will restrict as many of the six degrees of freedom as possible in order to facilitate the assembly and alignment [1][2].

The approach adopted for the OPS utilized a barrel approach, which constrained the cells to only two degrees of freedom: namely translation along, and rotation about the optical axis. In order to meet the tolerances set in the optical design, parameters such as centering of the optics within the cells, centering the fiber within the barrel, and the machining and mechanical tolerances, needed to be addressed during the design of the optomechanics. This chapter presents a comprehensive account of the OPS optomechanics, more specifically: the description of the OPS barrel is presented in section 5.1, the cell holders are described in section 5:2, and the fiber centering mechanism is provided in section 5.3.

5.1 OPS Barrel

As discussed in Chapter 2, to allow for easy system integration, the OPS had to be robust, modular, easy to assemble, and compact. Based on both the optical design described in the previous chapter, and the optomechanical design of the overall system demonstrator, a barrel assembly was employed to house the OPS components. A picture of the dismantled OPS is shown in figure F5-1, and the fully assembled OPS along with the outer barrel and the lenslet barrel is shown in figure F5-2. One of the advantages of the barrel was that all the optical components, except for the last surface of the second Fourier lens, were fully protected

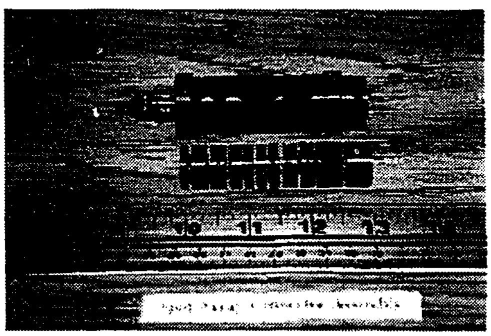

Figure F5-1: Photo of the Unassembled OPS

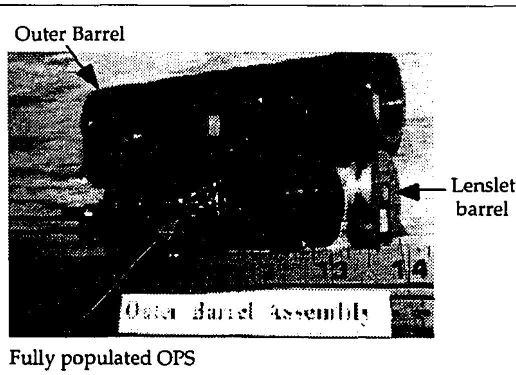

Figure F5-2: Photo of the Assembled OPS, the Lenslet Barrel, and the Outer Barrel

A 3-dimensional mechanical drawing of the OPS components, the OPS barrel, the outer barrel, and the lenslet barrel is given in figure F5-3, and a cross-sectional drawing of the assembled OPS is provided in figure F5-4.

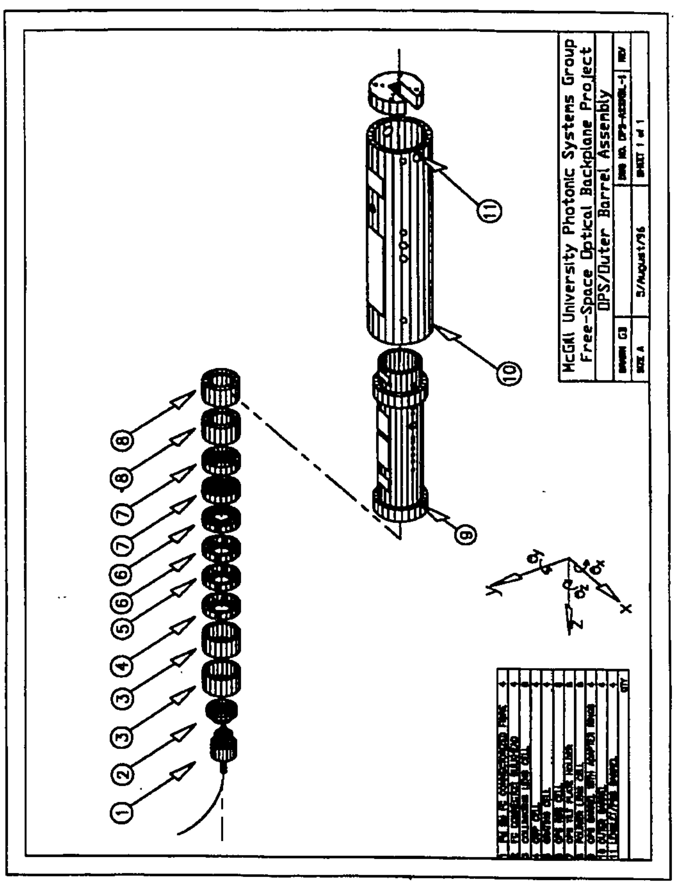

Figure F5-3: Mechanical Drawing of the OPS, the Lenslet Barrel, and the Outer Barrel

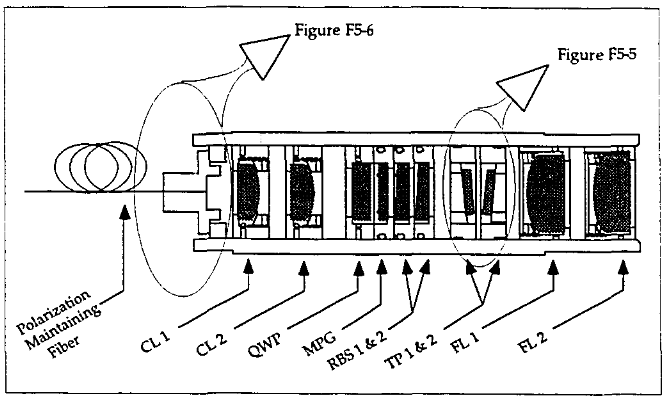

Figure F5-4: OPS Cross-Section

For ease of machining, the barrels were made out of aluminum, and subsequently anodized to increase the hardness of the aluminum surface. Two Delrin^{tm} (acetal) [see note A in Appendix C] rings were then press-fitted onto each barrel to facilitate its insertion into the respective outer barrel. Windows of width 12.6mm were machined at the top of the barrels to allow access to the optics' cell holders for alignment (most clearly shown in figure F5-3). Standard threaded holes (0-80 and 2-56) were machined along the two sides of the barrel such that steel set screws could securely hold each aligned optic in place. The thickness of the OPS barrel wall was 2.5mm ± 0.1mm.

5.2 Cell holders

The cell holders were machined to provide a sliding fit to the barrel. In order to provide access for alignment (in rotation about, and translation along the optical axis), eight holes along each cell's perimeter were machined. All the cells except those for the lenses and the tilt plates were fabricated entirely using anodized aluminum. The cells for the lenses were machined from Delrin^{tm} such that an interference fit between the cell and lens edge surfaces securely held each lens in place. Experimental validation on the positioning of the 50mm Fourier lens within its cell showed that only a 50μm circle was described by the focused spot when the cell was rotated about the axis of an input collimated He-Ne laser beam. The other (planar) optical elements were glued onto their respective aluminum cells using Norland UV curing glue #61.

One of the problems encountered with the cell holder design was that localized deformations about the screw/cell contact point occurred on the cell surface. The raised material about the contact point had the effect of reducing the sliding-fit clearance necessary, resulting in jamming. More sophisticated cells for the tilt plates which took this into consideration are shown in figure F5-5. The tilt plate cell incorporated a hybrid design of both Delrin^{tm} and anodized aluminum; Delrin^{tm} was used for the outer holder, and anodized aluminum for the inner holder. The anodized aluminum inner holder was machined at 10^{o} at the optic-metal interface. A groove along the perimeter of the outer holder provided the clearance necessary such that localized deformations about the screw/cell contact point did not cause the cell to get stuck within the barrel. The outer holder was machined to provide a tight interference fit with the inner holder.

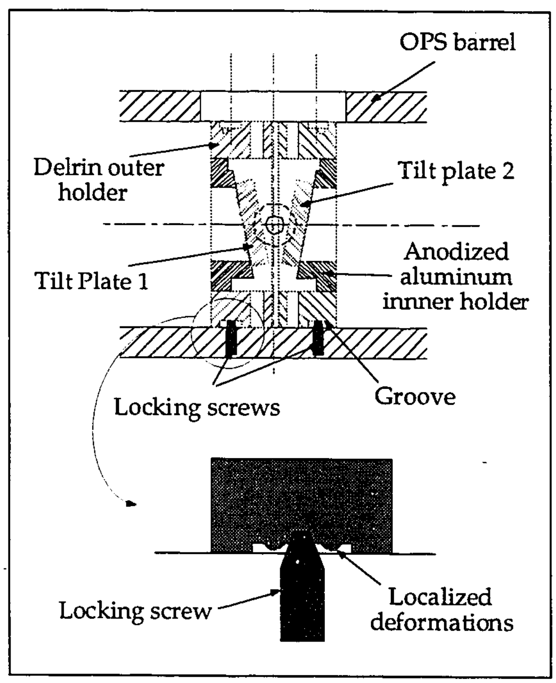

Figure F5-5: Tilt Plate Cell Holder

5.3 Fiber mount

A close-up of the mechanism to center the fiber to the optomechanical axis of the barrel is shown in figure F5-6. A high quality FC/PC fiber receptacle (Rifocs Corporation Part # MPC-108) was chamfered down at 45° into a circle of 15mm diameter. Butted up against the fiber receptacle bulkhead (made of anodized aluminum) which was locked into place in the barrel, four set screws were driven against the chamfered edge for lateral adjustment.

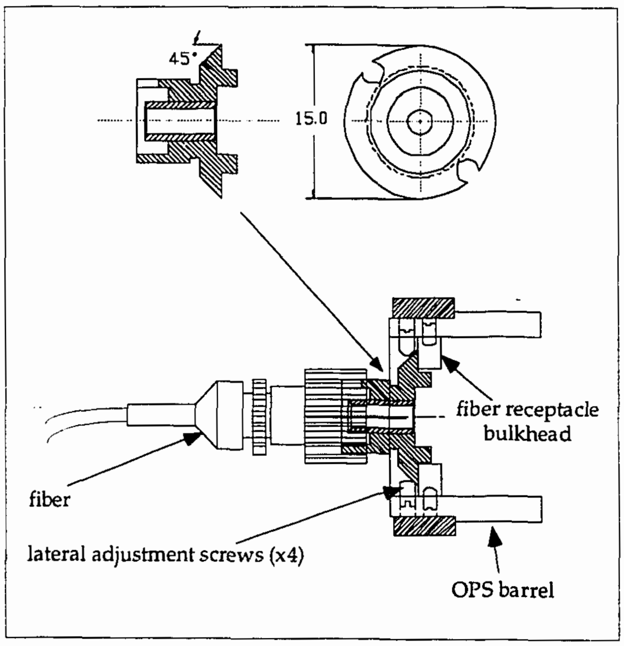

Figure F5-6: Fiber Mount Mechanism

The experimental setup for centering the fiber receptacle within the barrel is drawn in figure F5-7. The OPS barrel, with a fiber plugged into the fiber receptacle was placed on a V-groove. The surface of the fiber facet was imaged 1:1 using a 50mm lens positioned 100mm away. A CCD camera was fitted with a x10 microscope objective and calibrated (406 frame-grabbed pixels/500µm), to view the image. An iterative approach of rotating the barrel on the V-groove, observing the imaged fiber facet on a monitor, and re-adjusting the lateral positioning screws of the fiber receptacle resulted in fiber centering to better than 10µm from the optomechanical axis, well within the ±100µm design tolerance. Stability measurements were conducted on insertion and removal of the connectorized input fiber, and no measurable misalignment within the ±1µm measurement precision was observed.

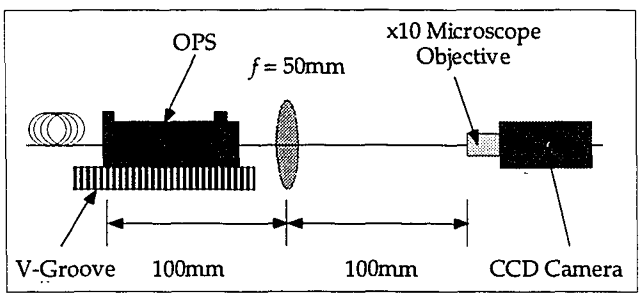

Figure F5-7: Fiber Centering Experimental Setup

5.4 Summary

Having described the optical design in the previous chapter, the optomechanics to house the OPS, namely the cell holders and the barrel were designed and manufactured to meet the original optomechanical requirements of simplicity, compactness and robustness. The next step was the assembly and the alignment of the optics within the OPS and will be described in the next chapter.

5.5 References

[1] M. Mizukami, K. Koyabu, M. Fukui, K. Kitayama, "Free-space optical module configuration using a guide-frame assembly method", Appl. Opt. **34**, 1783—1787, (1995).

[2] F. B. McCormick, F. A. P. Tooley, J. L. Brubaker, J. M. Sasian, T. J. Cloonan, A. L. Lentine, R. L. Morrison, R. J. Crisci, S. L. Walker, S. J. Hinterlong, and M. J. Herron, "Optomechanics of a free-space photonic switching fabric: the system," SPIE Optomechanics and Dimensional Stability, **1533**, 97—114 (1991).

CHAPTER 6 Assembly and Alignment

The assembly of the OPS was greatly simplified with the aid of an elegant custom made tool, called the OPS Insertion Slug. Alignment of the optics within the OPS required that adjustments be made to the positions of the collimating lenses and the Fourier lenses. Details on the experimental techniques used in the alignment procedures are presented in this chapter.

6.1 Assembly of the OPS

Assembly of the OPS was simplified by the use of the OPS insertion slug. The insertion slug was composed of three pieces: the rod, the ring, and the pin. By positioning the ring at the appropriate position on the rod by pushing the pin through accurately machined holes in the rod, each element could be inserted into the barrel from the output side of the barrel as shown in figure F6-1, until the ring butted up against the output end of the barrel. Component placement precision was better than ±90μm.

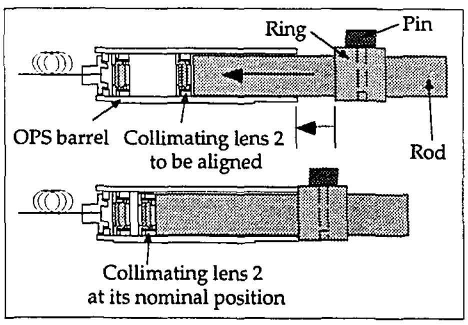

Figure F6-1: OPS Insertion Slug

6.2 Alignment of the OPS

A two step alignment sequence was required to assemble the components of the OPS within the barrel. In order to properly collimate the beam and to provide the correct spot size at the output of the OPS, adjustment of the two collimating lenses was required. In order to monitor both of these effects simultaneously, the OPS barrel with the pre-centered fiber was populated with only the 4 lenses positioned at their nominal positions using the insertion slug. The Fourier lenses were locked in place. The remaining 6 elements were not inserted, and in their place, a 50:50 beamsplitter was inserted through the barrel window, as shown in figure F6-2. The OPS was mounted onto a standard Spindler&Hoyer test-rig mount for the entire pre-alignment sequence.

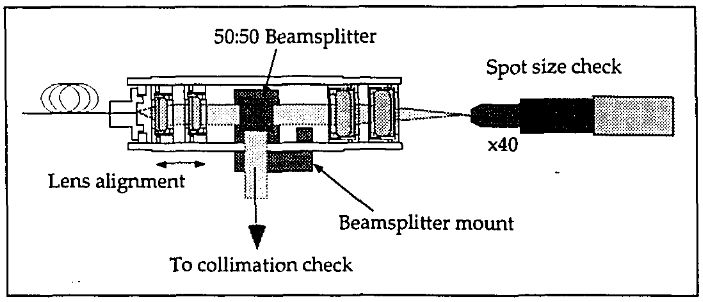

Figure F6-2: Alignment of the Collimating Lenses

'Real-time' spot size measurements were required due to the iterative approach used in the alignment technique, as will be further explained below. There are several methods to perform the measurements of 1 to 10μm spot sizes as explained in [1][2]. Unfortunately, these take a large amount of time to perform the measurement for the application at hand. A simpler method was used which was quick to perform, and which yielded acceptable results [3].

Spot size measurements were made using a linear high resolution CCD camera (Cohu 4815-5000) with a x40 microscope objective (Spindler & Hoyer Part #03-8714) with an NA of 0.45. The CCD camera was placed on a motorized xyz stage (Klinger Model # UT100-PP) which had a resolution of 1 μm in the direction of the optical axis, and 0.1μm along the other two axes.

The linearity of the CCD camera was calibrated by the following technique. At low laser power, a spot was imaged by the camera, and subsequently sent to a frame-grabber card in a computer. The maximum pixel value of the spot was recorded. By monitoring the maximum pixel value as the power was gradually increased, a relationship between the power and the response of the camera was obtained. The resulting response for the Cohu is shown in graph G6-1 below. Note that the linearity of the CCD trails off after pixel value of about 240. (Note the maximum saturation value was 255).

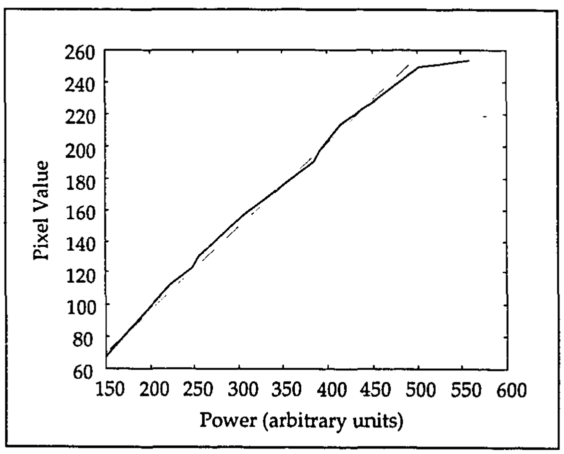

Graph G6-1: Linear Response of the Cohu 4815-5000 CCD Camera

Using a 10μm graticule, the CCD was calibrated to a measurement resolution of 2.509 frame-grabbed pixels/μm (i.e. 0.40μm/pixel) in the horizontal direction, and 2.4529 frame-grabbed pixels/μm in the vertical direction. The images of the spots were frame-grabbed and curve fitted (in both axes) to a Gaussian model from where the spot radii were obtained. With an iterative approach of setting the collimating lenses for collimation and measurement of the spot size, the ideal positions for the lenses were achieved. An explanation of the experimental setup that was used for the collimation check is provided in the next subsection.

Further processing of the spot size measurement by deconvolving the optical effects of the microscope objective, the CCD camera and the frame-grabber [4] were not found to be necessary as the spots that were generated were experimentally acceptable for the system. However, anticipating a convolution effect of at most 5%, the collimating lenses were placed in a position to yield a a spot size measurement slightly larger than the 6.47μm target, but still within the 0.25μm tolerance, to account for the convolution effect.

Once the collimating lenses were locked, the beamsplitter and the Fourier lenses were removed. Each barrel was then fully populated with the QWP, MPG, Risley prisms, the tilt plates, and the Fourier lenses, with the prisms and the tilt plates at their 'zero' positions. Alignment of the QWP was done in-situ after the OPS was integrated into the system to maximize transmission through the PBS-QWP assembly.

It should be noted that the locking of the collimating lenses modified the spot size by ±0.10μm on average.

Spot separation was set by adjusting the second Fourier lens measured using the same CCD setup with the x40 microscope objective (see Figure F6-2).

6.2.1 Collimation Check Experimental Setup

It was necessary to provide a means to monitor the beam propagating through the OPS barrel for collimation during the adjustments of the collimating lens pair. This was done by inserting a 10 x 10 x 10 mm 50:50 beamsplitter in the path of the beam to tap a part of the beam for observation (as was shown in figure F6-2). Validation of a beam's collimation is accomplished by many means (such as using a very long focal length positive lens and a CCD camera, or using a shear plate [5][6][7]). Another simple technique, the one that was employed for the OPS alignment, is described below.

As shown in figure F6-3, the beam reflected from the first beamsplitter (BS1) was issued 3.5 meters down the optical table to a (dielectric) mirror. Simultaneously, the beam was reflected via the second beamsplitter (BS2) to a second mirror. Both of the beams reflected from both mirrors were then reflected off or transmitted through (respectively) BS2 to a screen where they were observed (using a CCD camera with a camera objective lens). Adjustment of the collimating lenses, will have a drastic effect of the size of the viewed spot created by the long arm of the beam in comparison to that created by the short arm. Thus it was a sensitive real-time (visual feedback) method to adjust the lens positions for proper collimation. It should be noted that a Gaussian beam (ω_0 = 1.15mm through the OPS) diverges as it propagates (as per equation 9 from Chapter 4). Thus after propagating a total of approximately 7 meters, the long arm of the beam had a beam radius ω = 2.00mm (corresponding to a 2ω area of 12.67mm^2), while the beam radius of the short arm (having propagated approximately 30cm) was still only about ω = 1.15mm (corresponding to a 2ω area of 4.15mm^2). Thus the two lenses needed to be adjusted such that the area of the spot created by the long arm was about thrice the area of the spot created by the short arm.

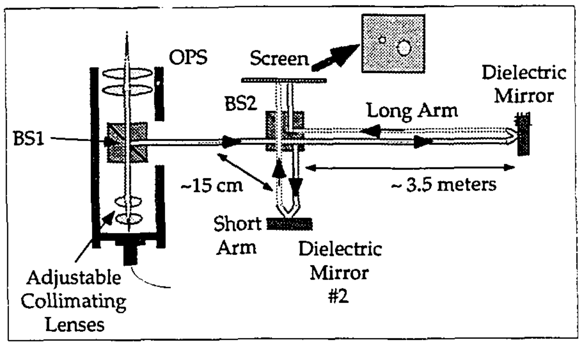

Figure F6-3: Collimation Check Experimental Setup

6.3 Summary

Due to the simple and elegant design of the optics and optomechanics of the OPS, assembly was greatly facilitated by the use of the OPS Insertion Slug. as well, alignment was relatively straightforward, yielding performance characteristics which met the requirements listed in Chapter 2. A full synopsis of the characterization results is provided in the next chapter.

6.4 References

[1] D. K. Cohen, B. Little, and F. S. Luecke, "Techniques for measuring 1-µm diam Gaussian beams", Appl. Opt. **23**, 637—640 (1984).

[2] M. B. Schneider, W. W. Webb, "Measurement of submicron laser beam radii", Appl. Opt. **20**, 1382—1388, (1981).

[3] Y.S. Liu, B. Robertson, D. V. Plant, H. S. Hinton, W. M. Robertson, "Design and Characterization of a microchannel optical interconnect for optical backplanes", accepted at Appl. Opt. (1996).

[4] G. L. Yip, P. C. Noutsios, and L. Chen, "Improved propagation-mode near-field method for refractive-index profiling of optical waveguides", Appl. Opt. **35,** 2060—2068, (1996).

[5] R. S. Sirohi, and M. P. Kothiayal, "Double wedge plate shearing interferometer for collimation test", Appl. Opt. **26,** 4054—4056 (1987).

[6] K. V. Sriram, M. P. Kothiayal, R. S. Sirohi, "Self-referencing collimation testing techniques", Opt. Eng., **32,** 94—100 (1993).

[7] De-Yan Xu, K. J. Rosenbruch, "Rotatable single wedge plate shearing interference technique for collimation testing", Opt. Eng., **30,** 391—396 (1994).

CHAPTER 7 Characterization

Detailed performance measurements were conducted on the four assembled barrels to obtain statistical information on the reproducibility of the design and implementation. The results are presented below. A frame-grabbed image of the spot array generated from barrel 1 is shown in figure F7-1. (Note that the image appears flipped in the horizontal direction in comparison to figure F2-7 due to the direction of observation, and the inversion introduced by the imaging optics and frame-grabber).

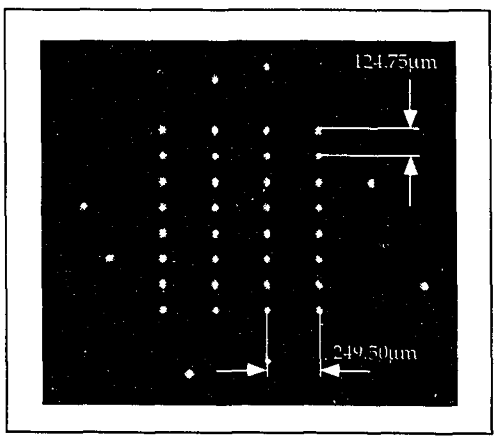

Figure F7-1: Frame Grab of the Generated Spot Array

7.1 Spots and Spot Array

As mentioned in Chapter 4, the frame-grabbed spots were curve fitted to a Gaussian beam model. This algorithm provided the $1/e^2$ irradiance spot size. It also calculated the Gaussian fit which was obtained by performing a chi-squared metric between the measured (quantized) data and the best-fit Gaussian curve [1][2]. The Gaussian fit program is given in Appendix B.

The characterization results for the four assembled and aligned OPS barrels is summarized in TableT7-1. For each barrel, the following information is presented as follows (with the measurement precision in parentheses): Average spot size, ω ($\pm 0.10\mu m$), and average Gaussian fit, %G of (a) the four central spots of an on-axis spot array, and (b) the four corner spots of an on-axis spot array. Note that the average axial position of the corner spots ($\pm 15\mu m$) is a direct measure of the field curvature introduced to the on-axis spot array (with the origin set at the average axial position for the four central spots). The measured spot size and Gaussian fit for a corner spot of a 685µm diagonally shifted spot array is also presented (685µm representing the maximum possible lateral shift achievable with the Risley prisms, as will be mentioned later in this section). The back focal length, BFL (i.e. the distance between the last lens surface to the spot array) is given ($\pm 0.1mm$) for each barrel. The last two columns in Table T7-1 respectively are the spot separation ($\pm 0.2\mu m$) and power uniformity ($\pm 1.0\%$). For convenience, the tolerances for the spot size, field curvature, back focal length, spot separation, and power uniformity are written in the headings of the appropriate columns.

It should be noted that any distortion (in spot separation) that was introduced was below the measurement precision of $\pm 0.2\mu m$, which is below the $\pm 0.57\mu m$ tolerance for 1% clipping, and therefore acceptable.

Power uniformity of the spot arrays were obtained from a frame-grabbed image using the linear high resolution Cohu 4815-5000 CCD camera (with automatic gain control turned off). The image was fed into a program which computed the integrated power (in pixel intensity units) per spot by summing the pixel elements within each spot's elementary cell (of 125μm by 250μm). Thus the total integrated power of each spot was measured and compared. This integration was necessary, since it was found to be difficult to match the plane of the spot array to the plane of the CCD active area directly, resulting in a spatially defocused image. Power uniformity measurements for barrels 1 and 2 were unavailable as they had already been integrated into the system at the time of this measurement. Noting the negligible statistical difference (to within measurement precision) between the measurements for barrels 3 and 4 however, it was expected that the MPGs for barrels 1 and 2 behave similarly, and the power uniformity was better than 92.0%.

Note, from Table T7-1, that all measurements but two fit within the specified tolerances. The spot size of an outer corner spot of a 685μm diagonally shifted spot array was measured to be 7.04μm for barrel 1, and 6.80μm for barrel 3, both larger than the allowable tolerance. Noting, however, that since the fiber was centered to better than 10μm within the OPS barrel (as presented in Chapter 5), compared to the ±100μm tolerance (as presented in Chapter 4), it was only be necessary to laterally shift the spot array by at most ±200μm and not 685μm. Thus these values were disregarded, as they were never reached when the OPS was integrated in the system.

OPS	Average center spot on-axis array		Average corner spot on-axis array			Corner spot of a 685μm shifted spot array		BFL	Separ-ation	Power Unif.
	ω	%G	ω	%G	z field curv.	ω	%G			
	6.47 ±0.25 μm		6.47 ±0.25 μm		<63 μm	6.47 ±0.25 μm		18.34 ±0.82 mm	125 ±0.57 μm	>90%
1	6.47	93.9	6.68	90.6	19	7.04	94.1	18.1	124.8	n/a
2	6.61	96.1	6.62	96.3	12	6.68	95.4	18.0	125.2	n/a
3	6.49	98.1	6.47	96.1	39	6.80	93.7	18.0	125.2	92.8
4	6.52	94.2	6.57	96.0	0	6.53	97.0	18.3	124.9	92.9

Table T7-1: Spot and Spot Array Characterization

7.2 Spectral Behavior

Observations using the TecOptics Spectrum Analyzer (Model # V3S23 driven with a Model # SA-1 Ramp Generator) indicate that backreflections from the components of the OPS do not have a noticeable impact on the spectral behavior of the laser. The Faraday isolator (figure F3-2) provided a nominal -40db of isolation and was required to achieve this performance.

7.3 Polarization

Measurements on the polarization stability of the light from the OPS were conducted. During pre-alignment, an OPS barrel was populated with only the two collimating lenses and the QWP as shown in figure F7-2. A PBS-QWP assembly (as mentioned in Chapter 2) was placed at the output of the OPS. The light transmitted through the PBS-QWP assembly is labelled as P_A and the unwanted leakage light, as P_B.

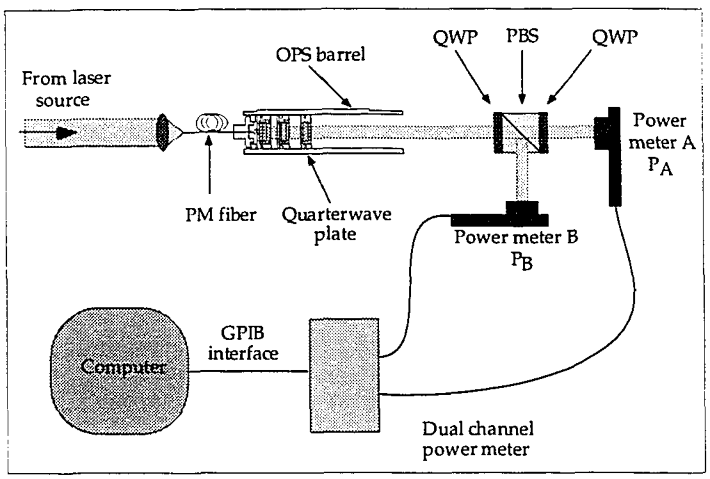

Figure F7-2: Polarization Stability Active Alignment Measurement Setup

By using an iterative computer-based 'real-time' visual feedback alignment technique (very similar to the technique used for optimally aligning the polarization of the light launched into the PM fiber as described in Chapter 3) fed from the dual-channel power meter, the orientation of the QWP within the OPS barrel was adjusted to produce light that maximized the ratio as given below in equation 26:

$$Throughput = \frac{P_A}{P_A + P_B}. \tag{26}$$

Measurements on the throughput through the PBS-QWP assembly was conducted. Maximum light throughput of 95.26% ±0.28% over time was measured using the ratio given in equation 26.

The non-ideal throughput of 95.26% was primarily incurred by the transmission efficiency of the PBS itself (specified to be 96.16% for p-polarization). The remaining 1% loss was due to the finite extinction ratio of the linearly-polarized light emitted from the PM fiber (measured to be 28dB), and imperfect orientation of the QWPs (the one within the OPS, as well as the two attached to the PBS by the supplier). Polarization stability is demonstrated by the ±0.28% time variation of the transmitted light.

7.4 Beam Steering

Measurement results conducted on the lateral steering travel of the Risley prisms on the spot array were ±685 (±3μm) from the optical axis. Measurement results on the angular steering coverage of the tilt plates were $\pm0.49^{\circ}(\pm0.08^{\circ})$. These values are better than the ±400μm and 0.46° lateral and angular steering requirements as specified in Table T2-1 to compensate for the alignment errors encountered during the integration of the OPS into the system.

7.5 Optical Power Budget

Measured throughput efficiencies were conducted on each of the optical elements of the OPS individually with a precision of ±0.5%. The values for barrel 3 are presented in the third column of Table T7-2, in relation to their expected (specified) values (columns 1 and 2 - reproduced from table T4-3). The final column in Table T7-2 shows the cumulative throughput efficiency after each element, based on the measured data from column 3, not including the MPG. It is shown that an overall throughput of 95.6% was expected, excluding the MPG.

The value for the efficiency of the MPG was determined indirectly after experimentally measuring the throughput of the entire OPS. The technique that was employed is presented in the next subsection.

Component	Estimated throughput efficiency	Cumulative throughput efficiency	Measured throughput efficiency	Calculated cumulative throughput efficiency based on measured values
Collimating lens 1	99.6%	99.6%	99.2%	99.2%
Collimating lens 2	99.6%	99.2%	99.2%	98.5%
Quarterwave plate	96.8%	96.0%	99.0%	97.5%
MPG	76.5%	73.5%	XXX%	XXX%
Risley prism 1	99.5%	73.1%	99.7%	97.2%
Risley prism 2	99.5%	72.7%	99.7%	96.9%
Tilt plate 1	99.5%	72.4%	99.7%	96.6%
Tilt plate 2	99.5%	72.0%	99.7%	96.3%
Fourier lens 1	99.6%	71.7%	99.6%	95.9%
Fourier lens 2	99.6%	71.4%	99.6%	95.6%

Table T7-2: Optical power budget characterization results

7.5.1 Measurement of OPS Throughput Efficiency

In order to remove the effects of power fluctuations of the laser on the measurements, the Newport 2832-c dual channel power meter was used. Since the Newport detector heads that were used (Model 818-ST/CM) require the area of the detector be maximally covered by the light (i.e. it is inaccurate in reading focussed spots), it was necessary to make each measurement with a collimated beam impinging the detector head.

In order to obtain the value of the total power in all the output spots with respect to the power emitted by the PM fiber at the input of the OPS, the following steps were performed:

- *Step 1:* Using an OPS outfitted with only 2 collimating lenses, the power of the output collimated beam was measured ($P_{A1}/P_B = 0.562$) as shown in figure F7-3. Thus the input power P_{IN} can be determined by dividing the measured efficiencies of the collimating lenses ($\eta_C = 0.992$).

$$\frac{P_{IN}}{P_B} = \frac{\left(\frac{P_{A1}}{P_B}\right)}{(\eta_C)^2} = \frac{0.562}{(0.992)^2} = 0.571 \qquad (27)$$

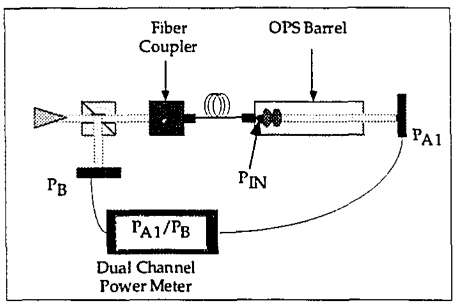

Figure F7-3: Step 1 — (P_{A1}/P_B)

- *Step 2:* A Spindler&Hoyer x20 microscope objective (Part # 03 8713) was used to collimate a focussed spot at the output of the OPS. In order to verify it's throughput efficiency (specified by the manufacturer to be 76.13% @ 850nm), two Fourier lenses were inserted in the OPS to focus the spot. The power of the collimated beam at the output of the microscope objective (P_{A2}/P_B) was measured to be 0.424, as shown in figure F7-4. Since the efficiency of the Fourier lenses were known a priori ($\eta_F = 0.996$), the efficiency of the objective could be found.

$$\frac{P_{A2}}{P_B} = \frac{P_{A1}}{P_B} \cdot (\eta_F)^2 \cdot (\eta_M) = 0.424 \qquad (28)$$

Thus, η_M was determined to 76.1% (a slight discrepancy with the quoted value).

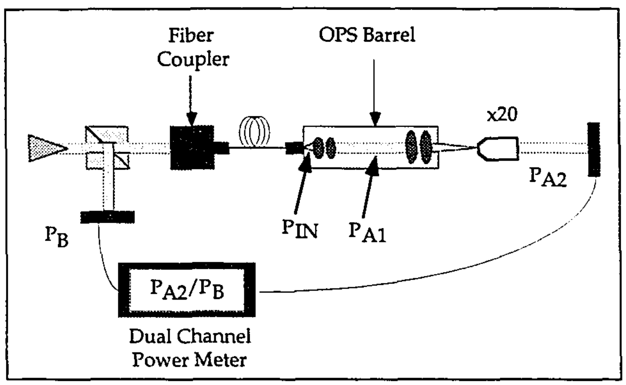

Figure F7-4: Step 2 — (P_{A2}/P_B)

- *Step 3:* The barrel was then fully populated as shown in figure F7-5. One of the spots of the spot array was collimated using the x20 microscope objective (P_{A3}/P_B), and measured to be 7.35e-3. According to the power uniformity program, this spot was 95.5% of the mean value of all the spots in the spot array. The power in one spot (P_{A4}/P_B) (on average) was then determined by:

$$\frac{P_{A4}}{P_B} = \frac{\left(\frac{P_{A3}}{P_B}\right)}{\eta_M} \cdot \frac{100}{95.5} = 10.1e-3 \tag{29}$$

Thus the total throughput efficiency of the OPS (P_{A4}/P_{IN})*40 (note the *40 multiplicative factor to include the total number of spots) was determined to be:

$$\frac{P_{A4}}{P_{IN}} \times 40 = \frac{\left(\frac{P_{A4}}{P_B}\right)}{\left(\frac{P_{IN}}{P_B}\right)} \times 40 = 0.709 \tag{30}$$

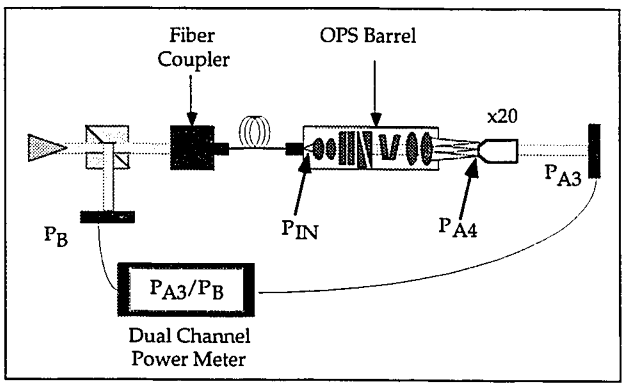

Figure F7-5: Step 3— (P_{A3}/P_B)

The estimated throughput efficiency of the OPS (last row in Table T7-2, column 3) was 71.4%. The actual measured value of 70.9% is only 0.7% lower than expected. With this validation of the overall throughput of the OPS, it was now possible to determine the diffraction efficiency of the MPG.

7.5.2 Diffraction Efficiency

In Chapter 4, the theoretical diffraction efficiency of the grating was given to be 76.5% (including the losses at both surfaces of 4%). Using the efficiency numbers for all the components from Table T7-2, the total throughput was:

$$\eta_{allbutMPG} = (\eta_C)^2 \cdot \eta_Q \cdot (\eta_R)^2 \cdot (\eta_T)^2 \cdot (\eta_F)^2 = 0.955 \tag{31}$$

Thus, dividing this value from the measured throughput of 70.9%, the derived diffraction efficiency of the MPG was:

$$\eta_{MPG} = \frac{\eta_{OPS}}{\eta_{allbutMPG}} = \frac{0.709}{0.955} = 0.742 \tag{32}$$

The result indicates that the diffraction efficiency of the MPG was slightly lower than the expected value of 76.5% by 3%. Errors in the fabrication are the probable source of this performance degradation.

A plot of the optical power budget appears in figure F7-6.

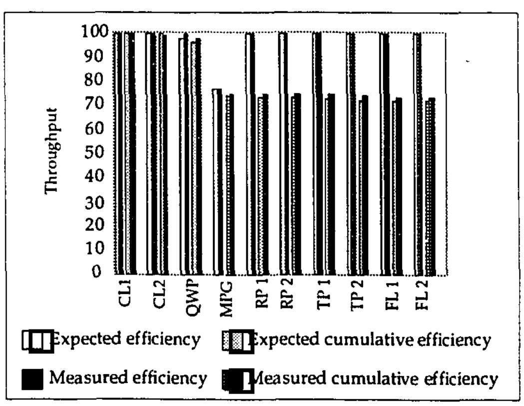

Figure F7-6: Plot of the Optical Power Budget - Expected and Measured

7.6 Summary

Characterization results that have been presented in this chapter show that the four OPS's that were built for the system demonstrator did indeed perform to system specifications. A discussion on the impact of the optical power generated by optical power supplies in general on modular based systems is presented in the next chapter.

7.7 References

[1] S. Wolfram, "Mathematica - A system for doing mathematics by computer", Addison-Wesley Publishing Company Inc, pp.587, 672 (1991).

[2] P. G. Hoel, "Elementary Statistics", John Wiley & Sons, Inc, pp. 54—67 (1962).

CHAPTER 8 Discussion

It is clear that in order for the current state of modulator based optoelectronics to establish a strong technical foundation from which to delve into research on the feasibility of photonics as a solution to the electronics bottleneck, efficient means of generating large arrays of high power spots must be made possible.

8.1 Increased Optical Power through the System

While the body of this thesis provided a thorough experimental account of the design, implementation and characterization of an OPS for a free space optical backplane, it is now wise to take a step back and delve into the effect that the optical power has on modulator based optoelectronic systems.

Optical power is the most crucial criteria in design of optical interconnects. Increased optical power results in a multitude of improved characteristics and relaxed design constraints; examples are listed below:

- More received power on the detector translates into a simpler receiver design; meaning lower electrical power consumption and therefore lower ambient chip operating temperature. Lower chip temperature will reduce the engineering efforts needed in thermal management.
- More optical power will increase switching times, and therefore an increased bit-rate, as shown below in graph G8-1. (This data is based on a single-rail design, operating at a bit error rate of 10^{-12} [1]).

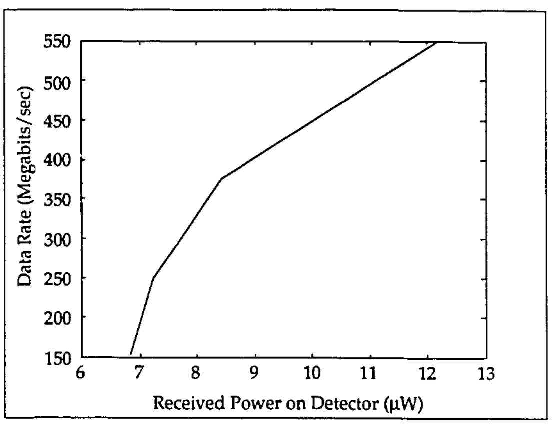

Graph G8-1: Data Bit Rate vs. Received Detector Power - Single Rail - (BER 10^{-12})

A similar plot is also shown in graph G8-2 for a dual-rail receiver design operating at a bit error rate of 10^{-14} [2].

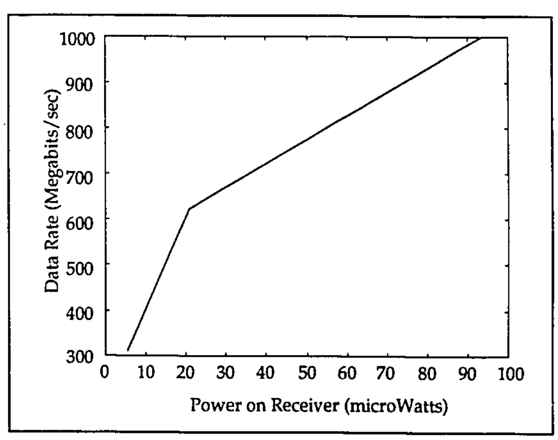

Graph G8-2: Data Bit Rate vs. Received Detector Power - Dual Rail - (BER 10^{-14})

- At a fixed data rate however, more optical power will therefore allow the chip designer to make the detector (and modulator) window sizes larger, relaxing the optics-to-chip alignment tolerances significantly.
- Larger window sizes means that larger, and thus more manageable beams need to be handled through the interconnect. Larger lenslet arrays or bulk optics, for example are easier to align with respect to one-another.
- Larger beam sizes relaxes the size of the size constraints generally imposed on free-space optical interconnect systems.
- Higher optical power lowers the need for expensive low-reflective optical components and highly efficient lenslet arrays and fan-out gratings (a binary phase grating is much cheaper than a more efficient multiple phase grating).
- More input optical energy reduces the need for extremely high quality modulators.

It should be noted that each of the above items correspond either directly or indirectly to a reduced overall cost in the system design, (not including the increased cost of supplying more optical power to the system), as well as reduced overall design time.

Thus we see that an increase in optical power supplied by an optical power supply extends the yardsticks that can be pushed in the research of free-space optical interconnects.

The cost of supplying highly controlled optical beams (i.e. spectra, polarization, power) does not come cheaply. For example, a 150mW CW Distributed Bragg Reflector laser diode (from Spectra Diode Labs) costs $3800 (US). Cheaper 200mW CW lasers without an internal grating are also available (from SDL) at $2000. Clearly, for industrial based applications demanding large arrays of beams (32 x 32), the cost of supplying the required optical power is prohibitive. For example, assuming a link efficiency of 60% between stages, a bit error rate of 10^{-14}, 100μW differential power incident on a receiver for a 1Gbit/sec operation (see

Graph G8-2), 70% efficiency of the OPS, and a modulator reflectivity 15% (low) and 30% (high), the necessary optical power required per stage would be 1.2W/ stage.

Projected improvements of both modulator and receiver performance [3] indicate that with a modulator reflectivity of 5% (low) and 95% (high), and a 1Gbit/sec receiver sensitivity of ~8μW, an estimate of only 21.7mW would be required per stage.

8.2 Array Scalability

In Chapter 4, section 4.2, the issue of spot array scalability was introduced. It was mentioned that if the pitch of the smart pixels were halved to utilize the unused modulators on the system's optoelectronic chip (i.e. a 16 by 8 array of modulators pitched at 62.5μm by 125μm), then only a simple redesign of the MPG would be sufficient to produce the new spot array. Technically, based on the compression ratio versus number of periods sampled (CR vs. NPS) argument provided in that section, it would technically be feasible to generate a 16 by 16 spot array, within the current optical and optomechanical design of the OPS, if the modulators were laid out on the chip on an even pitch of 62.5μm.

8.3 References

[1] A. V. Krishnamoorthy, T. K. Woodward, K. W. Goosen, J. A. Walker, A. L. Lentine, L. M. F. Chirovsky, S. P. Hui, B. Tseng, R. Leibenguth, J. E. Cunningham, and W. Y. Jan, "Operation of a single-ended 550Mbit/s, 41fJ, Hybrid CMOS/MQW receiver transmitter", Electronics Letters **32**, 764—766, (1996).

[2] T. K. Woodward, A. L. Lentine, L. M. F. Chirovsky, "1 Gb/s operation and bit-error rate studies of FET-SEED diode clamped smart-pixel optical receivers", IEEE Photonics Technology Letters **7**, 763—765, (1995).

[3] D. V. Plant, "Constructing a free-space optical backplane: Challenges and choices", presented at the *Optics in Computing Meeting* at the *1997 Spring Topical Meetings*, OThB1, March 18-22, Lake Tahoe, Nevada, 1997.

CHAPTER 9 Conclusion

This thesis presented an optically simple approach to drive an array of 32 Hybrid/SEED modulators for use in a four-stage optical interconnect, while illustrating two critical points: namely, (i) the optical design must be done in conjunction with the optomechanical design, and (ii) the design of the module must be done in conjunction with the optical and optomechanical design of the entire system.

The success of the design is based on meeting the specifications which were presented in Table T2-1. This table is presented again in Table T9-1 along with the characterization results. The power requirement (the eighth item in the list) was satisfied by taking into account measured optical losses encountered by the laser beam through the optical train (figure F3-2) of 74.8%, and loss at the fiber coupler which was at worst 50%. Based on the laser source providing 500mW, this results in spots at the output of the OPS of ~900μW, over 3 times the required power. It should be noted that the optical interconnect, i.e. light originating from the OPS through to the Hybrid/SEED chip on the first stage, through the optics to the Hybrid/SEED chip on the second stage, was established, demonstrating that the requirements for the OPS were satisfied.

OPS Spot array requirement	OPS characterization results for the 4 barrels
8 by 4 focused spots on a uniform grid of 125.00μm by 250.00μm (±0.57μm)	8 by 4 spots on a uniform grid. In vertical direction: min: 124.75μm; max: 125.15μm
8 additional alignment spots	Achieved through MPG design
Back focal length (bfl) of 18.34±0.82mm	Min bfl = 18.00; Max bfl = 18.30

Table T9-1: OPS Spot Array Requirements and Characterization Results

OPS Spot array requirement	OPS characterization results for the 4 barrels
$1/e^2$ irradiance spot radii of 6.47±0.25μm	Min center spot size = 6.47μm Max center spot size = 6.61μm Min corner spot size = 6.47μm Max corner spot size = 6.68μm
Slower than f/6 beams generating spot array	f/12 spots generated
Stable right hand circularly polarized light	Achieved in-situ
Minimal field curvature < 63μm across spot array	Min field curvature = 0.25μm Max field curvature = 38.75μm
Power per spot greater than 250μW	900μW per spot (see Chapter VIII)
Power uniformity across the entire array of greater than 90%	Array power uniformity >92%
Beam steering capabilities of greater than: ± 400μm lateral translation ± 0.46° angular deviation	Beam steering capabilities of: ±685μm lateral translation ± 0.49° angular deviation
Spectral tolerance of 850±1nm	850.0 ± 0.05nm

Table T9-1: OPS Spot Array Requirements and Characterization Results

Future optical interconnects will most probably employ the use of source based transmitters (e.g. VCSELs) rather than modulators. However, this is only foreseen to occur after a few years once VCSEL technology manages to produce large (64 x64) arrays of lasers co-integrated with CMOS, interlaced with detectors, with high optical uniformity, and low electrical drive requirements [1].

Thus, in the interim, the necessity for the advancement of R&D in this field requires simple, elegant, and practical optical solutions to meet the current state of affairs. This paper has shown that for the first time, a compact modularized spot array generator has been built for use in a modulator based optical interconnect, successfully taking the first step in bridging the generation gap between sophisticated Hybrid/SEED optoelectronics and optics.

9.1 References

[1] D. V. Plant, "Constructing a free-space optical backplane: Challenges and choices", presented at the *Optics in Computing Meeting* at the *1997 Spring Topical Meetings*, OThB1, March 18-22, Lake Tahoe, Nevada, 1997.

APPENDIX A OSLO Design Specs

Dominic Goodwill - University of Colorado (1995)

*LENS DATA

McGill Fiber to spot array plane

SRF	RADIUS	THICKNESS	APERTURE RADIUS	GLASS SPE	NOTE
0	--	5.617200	0.100000	AIR	
1	--	--	5.000000 A	AIR	
2	ELEMENT	4.200000	5.000000	SF56 C *	
4		--	5.000000	AIR	
5	--	5.485800	5.400000	AIR	
6	--	--	5.000000	AIR	
7	ELEMENT	4.200000	5.000000	SF56 C *	
9	P	--	5.000000	AIR	
10	--	7.000000 P	10.000000	AIR	
11	ELEMENT	3.250000	10.000000	BK7 C *	
12	Quarter wav	--	10.000000	AIR	
Quarter wave plate					
13	--	1.500000	10.000000	AIR	

14	ELEMENT	1.587500	10.000000	SILICA C *	
15	BPG active	--	10.000000	AIR *	

BPG active surface

16	--	2.000000	10.000000	AIR	
17	ELEMENT	2.000000	10.000000	SF10 C *	
18	Risley pris	--	10.000000	AIR	Risley prism
19	--	2.000000	10.000000	AIR	
20	ELEMENT	2.000000 P	10.000000	SF10 P *	
21	Risley pris	--	10.000000	AIR	Risley prism
22	--	7.000000	10.000000	AIR	
23	ELEMENT	3.000000	10.000000	SF10 C *	
24	Tilt plate	--	10.000000	AIR *	

Tilt plate to correct chief ray angle error at spot array plane

25	--	7.230600	10.000000	AIR
26	25.483000	5.000000	9.000000	BK7 C
27	-21.909000	1.500000	9.000000	F2 C
28	-139.240000	--	9.000000	AIR
29	--	5.240000	11.250000	AIR
30	25.483000 P	5.000000	9.000000	BK7 C

31	-21.909000	1.500000	9.000000	F2 C
32	-139.240000	--	9.000000	AIR
33	--	18.445217 S	5.000000	AIR
34	--	-0.120000	5.000000	

*PARAXIAL SETUP OF LENS

APERTURE

Entrance beam radius:	1.221300	Image axial ray slope:	-0.100971
Object num. aperture:	0.212458	F-number:	-34.163358
Image num. aperture:	0.098666	Working F-number:	5.067612

FIELD

Field angle:	-1.019898	Object height:	0.100000
Gaussian image height:	-0.215331	Chief ray ims height:	-0.216467

CONJUGATES

Object distance:	5.617200	Srf 1 to prin. pt. 1:	-127.817751
Gaussian image dist.:	18.445217	Srf 33 to prin. pt. 2:	281.580594
Overall lens length:	70.693900	Total track length:	94.636317
Paraxial magnification:	-2.153308	Srf 33 to image srf:	18.325217

OTHER DATA

Entrance pupil radius:	1.221300	Srf 1 to entrance pup.:	--
Exit pupil radius:	2.296903	Srf 33 to exit pupil:	41.193372
Lagrange invariant:	0.021742	Petzval radius:	-10.460685
Effective focal length:	-83.447417		

APPENDIX B Gaussian Fit Program

```
% This program takes a 2 dimensional array called 'A'

% This program is a modification to the program originally written by
% Yong Sheng Liu

% Modified by Rajiv Iyer
% Latest modification by Rajiv Iyer on Feb 6, 1997

% The A matrix is set by exporting the frame-grabbed spot
% as a text file, editting it with the characters :
% A=[
% prior to all the data, and :
% ];
% following all the data.
% The text file should be a .m file, so that it can be
% executed by MATLAB



cla;
clf;

w0=6;% wo is the first guess at the beamwaist
w1=1.5*w0;% w1 is a final guess at the beamwaist

delt_x=0;% force the gaussian fit to shift
delt_y=0;% delt < 0   -->   shift to the left!

% write the text file into matrix A

[m, n] = size(A);

peak = max(max(A));

B=A/peak;% normalization


% find the peak position (rw_max,clm_max) from the B;

peak=B(1,1);

for i=1:m
for j=1:n
if B(i,j) > peak
rw_max = i;
clm_max = j;
```

```
peak = B(i,j);
end
end
end

% normalize the matrix

% pick up the row and column which contains the peak
rw = B(rw_max, :);
clm = B(:, clm_max);

% Gaussian curve fitting

errfit_x=1000;
errfit_y=1000;

%=======xxxxxxxxxxxxxxxxxxxx=======%

%-----% fitting for row---x!
for w = w0 : w0/200 : w1
for i=1:n
j=-clm_max-delt_x+i;
    gauss_x(i)=exp(-2*j^2./(w.^2));
end

errfit_new_x=std(gauss_x-rw);
if errfit_new_x < errfit_x
errfit_x = errfit_new_x;
w_best_x = w;
end
end

% best Gaussian fitting for the row-cut:
for i=1:n
j=-clm_max-delt_x+i;
gauss_best_x(i)=exp(-2*j^2/(w_best_x^2));

end

% Gaussian fit metric
% ks stands for the Kolmogorov-Smirnov Test
%ref: p617 of "Numerical Recipies in Fortran
%- The art of Scientific Computing 2ndEd"
%William H. Press Saul A Teukolsky, William T. Vetterling
%Brian P. Flannery
% This book was borrowed from Professor Peter Kabal.


ks=0;
sum=0;
for i=1:n
diff=gauss_best_x(i)-rw(i);
sum=sum+diff^2;
```

```
if abs(diff)>ks
ks=abs(diff);
end
end
tmp=(sum)^(0.5);
x_metric1=(1-tmp)*100;
x_metric2=(1-sum)*100;
x_metric3=(1-ks)*100;



%=====yyyyyyyyyyyyyyyyyyyyyy======%

%-----% fitting for column---y!
for w = w0 : w0/200 : w1
for k=1:m
l=-rw_max-delt_y+k;
tpy(k)=l;
gauss_y(k)=exp(-2*l^2./(w.^2));

end

errfit_new_y=std(gauss_y-clm');
if errfit_new_y < errfit_y
errfit_y = errfit_new_y;
w_best_y = w;
end
end

% best Gaussian fitting for the column-cut:
for k=1:m
l=-rw_max-delt_y+k;
    gauss_best_y(k)=exp(-2*l^2/(w_best_y^2));

end


% Gaussian fit metric
ks=0;
sum=0;
for i=1:m
diff=gauss_best_y(i)-clm(i);
sum=sum+diff^2;

if abs(diff) > ks
ks=abs(diff);
end
end
tmp=(sum)^(0.5);
y_metric1=(1-tmp)*100;
y_metric2=(1-sum)*100;
y_metric3=(1-ks)*100;

fprintf('\n');
```

```
%fprintf('xfit1: %g.xfit2: %g. xfit3: %g.best_w_x: %g.\n', x_metric1,
x_metric2, x_metric3, w_best_x)
fprintf('xfit: %g %g %g.    best_w_x: %g.\n', x_metric1, x_metric2,
x_metric3,w_best_x)
%fprintf('yfit1: %g.yfit2: %g. yfit3: %g.best_w_y: %g.\n', y_metric1,
y_metric2, y_metric3, w_best_y)
fprintf('yfit: %g %g %g. best_w_y: %g.\n', y_metric1, y_metric2,
y_metric3, w_best_y)
w_avg=(w_best_x+w_best_y)/2;
fprintf('average w= %g\n', w_avg)

x_calib = 2.509;
y_calib = 2.4529;

wx=w_best_x/x_calib;
wy=w_best_y/y_calib;
wavg=(wx+wy)/2;

fprintf('with x calib %g, wx= %g\n', x_calib, wx)
fprintf('with y calib %g, wy= %g\n', y_calib, wy)
fprintf('average : %g\n', wavg)


% plot the curve of the row and column
subplot(2,1,1), plot(rw, 'g')
grid on
hold on
subplot(2,1,2), plot(clm, 'r')
grid on
hold on

subplot(2,1,1), plot(gauss_best_x, 'y')
subplot(2,1,2), plot(gauss_best_y, 'y')
xx=[0:0.1:300];
yy=sin(xx);
sound(yy)
break


% END
```

APPENDIX C Notes

[A] PANDA^{tm}, Polarcor^{tm}, and Delrin^{tm} are trademarked names. The mention of these brand names in this paper is for information purposes only and does not constitute an endorsement of the products by the author or McGill University.

Rev 3 02/03/97

Submitted to Applied Optics, March 1997

Design, Implementation, and Characterization of an Optical Power Supply Spot Array Generator for a Four Stage Free-Space Optical Backplane

R. Iyer, D. J. Goodwill[1], W. M. Robertson[2], D. V. Plant, M. H. Ayliffe, G. C. Boisset, D. Kabal, F. Lacroix, Y. S. Liu, B. Robertson

Department of Electrical Engineering
McGill University
Montréal, Québec, Canada
http://www.photonics.ee.mcgill.ca

[1] University of Colorado, Boulder, CO
[2] Middle Tennessee State University, Murfeesboro, TN

ABSTRACT

The design and implementation of a robust, scalable and modular optical power supply spot array generator for a modulator-based free-space optical backplane demonstrator is presented. Four arrays of 8 by 4 spots of ($1/e^2$ irradiance) 6.47μm radii pitched at 125μm in the vertical direction and 250μm in the horizontal were required to provide the light for the optical interconnect. Tight system tolerances demanded careful optical design, elegant optomechanics, and simple but effective alignment techniques. Issues such as spot array generation, polarization, power efficiency, and power uniformity are discussed. Characterization results are presented.

KEY WORDS

optical power supply, spot array generator, modulators, SEEDs, optomechanics, optical design, alignment, module, characterization

I. Introduction

Current high performance switching and computing systems rely mainly on electrical interconnection networks to transport information from chip-to-chip and board-to-board. However, electrical interconnects are limited by bandwidth, connectivity, power consumption, and latency constraints. Because the aggregate bandwidth of the integrated circuits inside these systems continues to increase, so must the capabilities of the interconnection network [1][2]. The intrinsic limitations of electrical interconnection networks has led system designers to consider short-distance optical interconnects as a way of increasing their performance [3—13]. The optoelectronic technologies being considered include two-dimensional arrays of both surface-emitting and modulator-based devices integrated with arrays of electronic processing elements, called Smart Pixel Arrays (SPAs). A class of SPAs well suited for optical backplane interconnection applications utilizes the Hybrid-SEED technology. This technology combines Quantum Confined Stark Effect (QCSE) modulators and PIN photodiodes (GaAs) with underlying silicon processing electronics [14] [15].

Because this type of smart pixel operates in the transmit mode by modulating an incident beam, systems utilizing this technology require optical power supply beams in order to power these reflective devices. The current state of affairs shows that there is a generation gap between the evolution of the sophisticated optoelectronics versus the optics necessary to drive them. Recently, we have constructed a four stage optical backplane demonstration system utilizing Hybrid-SEED SPAs [7] to address this problem. This paper describes the design, implementation and characterization of an optical

power supply spot array generation system built to bridge this generation gap. The full description of the optical design for the system was described in reference [16], and the optomechanical design in reference [17].

The paper begins by describing the requirements for the optical power supply (OPS) in Section II. The light source and distribution are explained in Section III. Section IV describes in detail the optical design, and Section V the optomechanics. The assembly and alignment methodology, and a final section on characterization results are provided in Sections VI and VII respectively.

II. Optical Power Supply Requirements

A. System Overview

The system was built in a three-dimensional layout interconnecting four hybrid-SEED smart pixel arrays in a unidirectional ring [7]. The chips were obtained through the ARPA/CO-OP/AT&T workshop [18]. A schematic of the unfolded optical layout of the system is shown in figure 1. (This figure is slightly misleading since the printed circuit boards should lie in the plane of the page and the optical power supplies perpendicular to the page). The optical interconnect was polarization based, and routes the optically encoded data from one stage to the next via polarization optics. A close-up of one stage is illustrated in figure 2. The focused spot array generated by the optical power supply was first collimated by the micro-lenses (125μm x 125μm) of the first pixelated-lenslet array (LA1). The light comprising the spot array needed to be right-hand circularly-polarized such that after passing through the first quarterwave plate (QWP1) (oriented at 45° in the x-y plane), it became linearly (p-) polarized. After passing through the polarizing beam splitter (PBS), and the second quarterwave plate (QWP2) which re-circularized the polarization, the beam array was then focused onto the Hybrid/SEED smart pixel device array residing on the printed circuit board (PCB) by the second lenslet array (LA2).

The reflected (modulated) light was then re-collimated through the lenslet array (LA2), and its polarization linearized to s-polarization through QWP2. Entering the PBS, the s-polarized light then reflected off the PBS mirror, to be routed to the next stage.

Figure 2 also illustrates the light relayed from the previous stage. This light, still s-polarized reflected off the PBS mirror surface toward LA1, after passing through the QWP1 which circularized its polarization. The beams then hit the pixellated mirrors on LA1, and passed through the same optical path as did the light from the OPS (as described above). The relayed beams however are displaced (in the x direction) 125μm away from the OPS beams, thus impinging receivers (as opposed to modulators) on the Hybrid/SEED SPA.

It should be noted for future reference that the QWP1, PBS, and QWP2 were pre-glued into what was collectively called the PBS-QWP assembly. The PBS-QWP assembly, LA1 and LA2 were mounted onto an optomechanical housing called the lenslet barrel, which, along with the OPS module resided within a larger housing called the outer barrel.

B. Spot Array Requirements

The layout of the 16 dual-rail smart pixels (i.e. 32 modulators) on the chip [15] were on an 8 by 4 grid pitched 125μm in the vertical direction and 250μm in the horizontal direction. The 32 modulator windows had a dimension of 20μm by 20μm and represent the targets for the spot array having passed through the PBS-QWP assembly and the lenslets. The requirements of the spot array at the output of the optical power supply, in order to hit the target modulators on the chip is given in Table 1, and a schematic of the desired spot array (looking in the direction of light propagation) is shown in figure 3. It should be noted that in figure 3, the central grid of 8 by 4 represent the signal spots, while the those on the periphery correspond to alignment spots. Although the requirements listed in Table 1 suffice for the designed system demonstrator, it was desired that the optical design be flexible to accomodate a larger array of target modulators for scalability.

C. Optomechanical Requirements

The system was built upon a vertically mounted baseplate housed in a standard 19" 6U VME commercial backplane chassis [19]. Based on the high level of integration, the optical power supply modules needed the following features:

- compactness
- robustness
- ease of assembly
- modularity

III. Light Source

As shown in figure 1, the system was a four stage optical backplane, with each stage requiring an OPS to provide the array of constant optical power beams to illuminate the modulators on the respective Hybrid/SEED chip. For simplicity, optomechanical compactness, and ease of pre-alignment, light was launched into the OPS via a single mode polarization maintaining fiber. For practicality purposes, a single 500mW tunable laser (with an external grating for wavelength selection and stabilization) was used to provide the light for all four stages. The light was originally split to the four stages by using a tree of three 1:2 fiber splitters. However, due to power loss and polarization instabilities, this arrangement was rejected. A second arrangement was employed using three thin membrane (linear-polarization preserving) pellicles, as shown in figure 4, which incurred no significant power losses nor polarization instabilities. Each beam was subsequently coupled into a 1m polarization maintaining (PM) single mode fiber to provide the optical inputs to each OPS module. Launching light along the PM fiber's fast axis was experimentally verified to provide better polarization stability at the output compared to launching along its slow axis. A Faraday isolator was used to eliminate backreflections into the laser.

Spectral tolerance was maintained to 850.0±0.05nm which was sufficient (by an order of magnitude) for the ±1nm spectral tolerance demanded by the SEEDs.

IV. Optical Design

The fundamental challenge in designing the OPS was in the generation of the array of 8 by 4 (+ 8 alignment) spots such that the 6.47μm ($1/e^2$ irradiance) radii spots were accurately positioned across the 125μm grid with uniform power distribution. There exist numerous techniques for producing spot arrays from a single beam [20][21]. Our system employed Fourier-plane array generation, utilizing a computer generated hologram implemented as a multiple level phase grating (MPG).

A. Multiple Level Phase Grating Design

The MPG was designed using a simulated annealing algorithm [21][22] to create a grating composed of a periodic array of unit cells that could generate the desired spot array in the focal plane of a Fourier transform lens; the grating itself representing the 2-dimensional spatial inverse Fourier transform of the spot array and placed at the front focal plane of the Fourier lens.

The periodicity, P, of the grating is related to the spot spacing, S, in the Fourier plane (i.e. the output focal plane of the Fourier lens), by the relation given in equation 1, where λ is the wavelength and f is the focal length of the Fourier lens. The factor 2 in the formula arises because only even order spots were used in the grating design.

$$P = \frac{2 \cdot f \cdot \lambda}{S} \qquad (1)$$

For the system demonstrator requiring a spot spacing of S=125μm (on the smallest grid as shown in Figure 3) for the array of 8 by 4 spots, and based on the chosen optical design, each unit cell had a periodicity of P = 377.8μm by 377.8μm, divided into 128 by

128 pixels as shown in figure 5. Each square pixel had a dimension of $P/128 = 2.95\mu m$ by $2.95\mu m$, and had a height quantized to one of 8 levels. The MPG was made from fused silica and was not anti-reflection coated due to time constraints.

From the design program, the theoretical efficiency of the 8 level phase grating was predicted to be 83% (76.5% after the 4% reflections at each non-AR coated surface). The overall uniformity of the spots was predicted to be 96.9%, defined using the metric:

$$Uniformity = 1 - \frac{(P_{max} - P_{ave})}{P_{ave}} = 1 - \frac{(P_{ave} - P_{min})}{P_{ave}} \approx 1 - \frac{(P_{max} - P_{min})}{P_{max} + P_{min}}, \quad (2)$$

where $P_{ave} = (P_{max} + P_{min})/2$.

Defining the collimated beam diameter passing through the MPG to be ω_{bpg}, the number of MPG periods sampled, NPS, is defined to be:

$$NPS = \frac{2\omega_{bpg}}{P}. \quad (3)$$

Also, from Gaussian beam propagation models, the focused spot radius, ω_f, is related to the collimated beam diameter by:

$$\omega_f = \frac{f \cdot \lambda}{\pi \cdot \omega_{bpg}}, \quad (4)$$

where f is the focal distance of the Fourier lens, and λ is the wavelength.

The (linear) compression ratio, CR, can be defined as the ratio of the spot separation to the 99% spot diameter:

$$CR = \frac{S}{3\omega_f}. \quad (5)$$

Thus, substituting equations 1, 3, and 4 into equation 5, a relationship between the compression ratio and the number of periods sampled is derived to be:

$$CR = \frac{\pi}{3} NPS \quad . \quad (6)$$

The number of periods sampled was NPS=6.1, where ω_{bpg} was designed to be 1.15mm, yielding a compression ratio of 6.37 through the relation given in equation 6 [23]. This value is sufficiently larger than the minimum CR_{min} of 3 which is required to ensure that the power uniformity is not degraded by aliasing [24].

The issue of scalablity was addressed by ensuring that a spot array of 16 by 8 spots at one-half the spot spacing (i.e. S=62.5μm) be implemented by replacement of the MPG element alone, with no other modifications to the optical design. Based on this requirement, the period P of the MPG would be doubled, thereby reducing the NPS to a value of 3.05. This results in a CR of 3.19, which is still larger than the CR_{min} of 3.

B. Optical Design

The optics were designed to meet all the spot array requirements while reducing the optomechanical complexities to a minimum, and is schematically shown in figure 6.

Perfectly linearly-polarized light was assumed to be emitted from the single mode polarization maintaining (PM) fiber placed at the front focal plane of the compound collimating lens (CL1, CL2). The mode field diameter ($1/e^2$ irradiance) of the fiber was specified to be 5.6μm. The collimated beam diameter at the output of the collimating lens was designed to be 2.30mm. After passing through the zero-order quarterwave plate (QWP) to right-hand circularize its polarization, the beam was then passed through the MPG. The angularly diffracted collimated beams then propagated through the Risley beam steerers (RBS 1 & 2) and tilt plates (TP 1 & 2) until they were focused by the compound Fourier lens (FL 1, FL 2) to spots in the Fourier plane of ($1/e^2$ irradiance) radii of 6.47μm.

Two-element compound lenses with variable focal lengths were chosen for both the Fourier lens and the collimating lens to account for uncertainties in the mode field diameter of the input fiber, the lens focal length specifications, and aberrations of the beams through the OPS. The lenses were oriented in the Petzval configuration [25] which provided the best performance in terms of aberrations, flexibility, optical power division, size, and cost. In the Petzval configuration, the optical power is split equally between the two parts of each compound lens. Hence the aberration is minimized, and the focal length of the lens is easy to adjust with high resolution by altering the air gap. Although a Plossl configuration is similar, simulations showed that in our application, the Petzval configuration gave lower aberrations for each spot. A Cooke's triplet, which has been used in an earlier modulator array application [26][27], was another option for the Fourier lens due to its exceptionally flat field. However, commercial Cooke's triplets have their focal length specified to only ±1%, compared to 0.4% required for the OPS optical design to define the correct spot separation. Since the optical power in a Cooke's triplet is divided very unequally across the three elements, adjusting the focal length requires extremely fine changes to the element spacings.

At their nominal (Petzval configuration) positions, the compound collimating lens had a focal length of 12.90mm, and the compound Fourier lens had a focal length of 27.78mm.

It should be noted that although a true Fourier lens should introduce $f\cdot\sin\theta$ distortion, at the maximum diffracted angle designed to be 0.0068° within the OPS, the small angle approximations hold. Therefore, an off-the-shelf lens pair was used due to cost and convenience.

Based on the nominal numbers used in the optical design, the speed (f/#) of the focused beams at the output of the OPS was f/12.07 ($1/e^2$ irradiance diameter of 2.30mm). This is well within the f/6 window demanded by the lenslets.

The OPS optical and optomechanical design had a number of optical and mechanical degrees-of-freedom in order to meet the set of design requirements; these are presented in table 2.

By analysis of these optical and optomechanical degrees-of-freedom, as well as the OPS module requirements listed in Section II, a barrel design was chosen to house the elements of the OPS. More information about the optomechanical design will be presented in Section V.

C. Design Tolerancing and Simulation

The total estimated lateral error of the position of the spot array with respect to LA1 (figure 2) was ±400μm. This value was calculated from the worst-case estimate of the fiber centering within the OPS barrel of ±100μm, which results in a ±230μm error of the spot array at the output of the OPS. As well, due to the accuracy to which the OPS barrel could be inserted in the outer barrel with respect to the LA1, machining tolerances, and centering of the lenses, an additional ±170μm lateral positioning error results. This corresponds to a 0.54° minimum required wedge angle for the Risley prisms (SF10 glass). Wedge angles of 1° were chosen due to availability and cost.

Angular misalignment of the fiber input was estimated to be 1° in the worst case yielding a 0.46° angular deviation from the optical axis of the chief rays of the output spots. To compensate for this misalignment, a 3mm thick tilt plate (SF10 glass) oriented at 10.4° with respect to the optical axis was required. Traditional tilt plate design requires one parallel planar optical element to have rotational degrees-of-freedom along the two axes perpendicular to the optical axis (pitch and yaw). This approach was not well-suited for the barrel housing chosen for the OPS, which only conveniently provides optomechanical degrees-of-freedom in translation along the optical axis, and rotation about the optical axis (roll). Therefore a novel two-element tilt plate design was implemented that requires only one degree of freedom, namely roll. Angular coverage of the spot array across the Fourier plane was achieved by permanently mounting two 1.5mm thick tilt plates (SF10 glass) at a fixed angle of 10° (from the optical axis), and by appropriately positioning both elements in roll.

Gaussian beam power clipping due to the square apertures of the system (lenslets and modulator windows) of 0.54% was taken into account in the optical design. A full analy-

sis of beam propagation through the optical interconnect showed that a 1% clipping effect is tolerable as long as the spot size is kept within tight tolerances.

The system was modelled using OSLO-Pro. Distortion of the spot array from the correct grid, field curvature, spot size variation, Strehl ratio, 1/RMS OPD, and the variations of the chief ray angles were calculated. The spot size was estimated in OSLO-Pro as the point spread function at the plane of best focus (minimum RMS OPD). In the point spread function calculation, a Gaussian apodization was applied at the first surface of the collimating lens. The width of this Gaussian function was given by a paraxial Gaussian calculation starting from a waist at the fiber facet.

Based on lateral adjustment provided by the Risley prisms, the simulation was carried out taking into account a maximum lateral displacement of the spot array of 575μm. Table 3 shows a summary of results of the simulation using the nominal design parameters as shown in figure 6. For each simulation, the calculated number for a spot located directly on the optical axis, for a corner signal spot of an on-axis spot array, and for a spot located 1152μm away from the optical axis (representing the outer corner spot of a 575μm diagonally shifted spot array) is given, along with the allowable tolerance values (shaded for clarity) based on 1% clipping of the beams by the modulator windows (on the Hybrid/SEED chip as shown in figure 2). Note that the tolerances for the minimum Strehl ratio and wavefront 1/RMS variation (1/RMS OPD) were set at 0.8 and 14 respectively [1, p 271][28].

It is shown in the table that all simulation results but one, for distortion, field curvature, spot size, chief ray angle, Strehl ratio, and wavefront 1/RMS variation fall within the tolerance limits for clipping of 1%. (Note that both the wavefront 1/RMS variation and Strehl ratio tolerances represent the minimum acceptable value). The spot size for the 1152μm diagonally shifted spot shows a simulation result of 6.75μm, which is 0.03μm larger than the maximum tolerance. As will be shown in Section V and VII, it was not necessary to displace the spot array this far.

Note that the ±2.5μm distortion tolerance represents the maximum diagonal distortion for the corner spots, which corresponds to a tolerance on the spot separation of 125.00 ± 0.54μm.

D. Optical Power Budget

The shaded columns of Table 4 show the estimated impact each component had on the overall throughput efficiency of the OPS. The table shows that the total excess losses (not including fan-out losses) were estimated to be 100% - 71.4% = 28.6%; while the losses not including the MPG were estimated to be only 2.9%.

V. Optomechanical Design

A. OPS barrel

As discussed in Section II, to allow for easy system integration, the OPS had to be robust, modular, easy to assemble, and compact. Based on both the optical design described in the previous section, and the optomechanical design of the overall system demonstrator, a barrel assembly was employed to house the OPS components. A picture of the disman-

tled OPS is shown in figure 7, and the fully assembled OPS along with the outer barrel and the lenslet barrel is shown in figure 8. One of the advantages of the barrel was that all the optical components, except for the last surface of the second Fourier lens, were fully protected. A 3-dimensional mechanical drawing of the OPS components, the OPS barrel, the outer barrel, and the lenslet barrel is given in figure 9, and a cross-sectional drawing of the assembled OPS is provided in figure 10.

For ease of machining, the barrels were made out of aluminum, and subsequently black anodized. The black anodization served to increase the hardness of the aluminum surface and to reduce any unwarranted glare. Two Delrin™ (acetal) [note A] rings were then press-fitted onto each barrel to facilitate its insertion into the respective outer barrel. Windows of width 12.6mm were machined at the top of the barrels to allow access to the optics' cell holders for alignment (most clearly shown in figure 9). Standard threaded holes (0-80 and 2-56) were machined along the two sides of the barrel such that steel set screws could securely hold each aligned optic in place. The thickness of the OPS barrel wall was 2.5mm ± 0.1mm.

B. Cell holders

The cell holders were machined to provide a sliding fit to the barrel. In order to provide access for alignment (in rotation about, and translation along the optical axis), eight holes along each cell's perimeter were machined. All the cells except those for the lenses and the tilt plates were fabricated entirely using anodized aluminum. The cells for the lenses were machined from Delrin™ such that an interference fit between the cell and lens edge surfaces securely held each lens in place. Experimental validation on the positioning of the 50mm Fourier lens within its cell showed that a 50μm circle was described by the focused spot when the cell was rotated about the axis of an input collimated He-Ne laser beam.

One of the problems encountered with the cell holder design was that localized deformations about the screw/cell contact point occurred on the cell surface. The raised material about the contact point had the effect of reducing the sliding-fit clearance necessary, resulting in jamming. More sophisticated cells for the tilt plates which took this into consideration are shown in figure 11. The tilt plate cell incorporated a hybrid design of both Delrin[tm] and anodized aluminum; Delrin[tm] was used for the outer holder, and anodized aluminum for the inner holder. The anodized aluminum inner holder was machined at 10° at the optic-metal interface. A groove along the perimeter of the outer holder provided the clearance necessary such that localized deformations about the screw/cell contact point did not cause the cell to get stuck within the barrel. The outer holder was machined to provide a tight interference fit with the inner holder.

C. Fiber mount

A close-up of the mechanism to center the fiber to the optomechanical axis of the barrel is shown in figure 12. A high quality FC/PC fiber receptacle was chamfered down at 45° into a circle of 15mm diameter. Butted up against the fiber receptacle bulkhead (made of anodized aluminum) which was locked into place in the barrel, four set screws were driven against the chamfered edge for lateral adjustment. Centering to better than 10μm

from the optomechanical axis was achieved, well within the ±100μm design tolerance. Stability measurements were conducted on insertion and removal of the connectorized input fiber, and no measurable misalignment within the ±1μm measurement precision was observed.

VI. Assembly and Alignment

The first stage of the alignment procedure was to launch the linearly-polarized light into each PM fiber along its fast axis using a computer-based active alignment technique. This was achieved by rotation of the halfwave plate (as shown in figure 4).

Assembly of the OPS was simplified by the use of the OPS insertion slug. The insertion slug was composed of three pieces: the rod, the ring, and the pin. By positioning the ring at the appropriate position on the rod by pushing the pin through accurately machined holes in the rod, each element could be inserted into the barrel from the output side of the barrel as shown in figure 13, until the ring butted up against the output end of the barrel. Component placement precision was better than ±90μm.

A two step alignment sequence was required to assemble the components of the OPS within the barrel. In order to properly collimate the beam and to provide the correct spot size at the output of the OPS, adjustment of the two collimating lenses was required. In order to monitor both of these effects simultaneously, the OPS barrel with the pre-centered fiber was populated with only the 4 lenses positioned at their nominal positions using the insertion slug. The Fourier lenses were locked in place. The remaining 6 elements were not inserted, and in their place, a 10mm 50:50 beamsplitter was inserted through the windows as shown in figure 14. The OPS was mounted onto a standard Spindler&Hoyer test-rig mount for the entire pre-alignment sequence.

Spot size measurements were made using a linear high resolution CCD camera with a x40 microscope objective with an NA of 0.45 [23]. The CCD camera was placed on a motorized xyz stage which had a resolution of 1μm in the direction of the optical axis, and 0.1μm along the other two axes.

Using a 10μm graticule, the CCD was calibrated to a measurement resolution of 2.509 frame-grabbed pixels/μm (i.e. 0.40μm/pixel) in the horizontal direction, and 2.4529 frame-grabbed pixels/μm in the vertical direction. The images of the spots were frame-grabbed and curve fitted (in both axes) to a Gaussian model from where the spot radii were obtained. With an iterative approach of setting the collimating lenses for collimation and measurement of the spot size, the ideal positions for the lenses were achieved.

Once the collimating lenses were locked, the beamsplitter and the Fourier lenses were removed. Each barrel was then fully populated with the QWP, MPG, Risley prisms, the tilt plates, and the Fourier lenses, with the prisms and the tilt plates at their 'zero' positions. Alignment of the QWP was done in-situ after the OPS was integrated into the system to maximize transmission through the PBS-QWP assembly.

It should be noted that the locking of the collimating lenses modified the spot size by ±0.10μm on average.

Spot separation was set by adjusting the second Fourier lens measured using the same CCD setup with the x40 microscope objective.

VII. Characterization

Detailed performance measurements were conducted on the four assembled barrels to obtain statistical information on the reproducibility of the design and implementation. The results are presented below. A frame-grabbed image of the spot array generated from barrel 1 is shown in figure 15. Note that the image appears flipped in the horizontal direction in comparison to figure 3 due to the direction of observation, and the inversion introduced by the imaging optics and frame-grabber.

A. Spots and Spot Array

As mentioned in Section VI, the frame-grabbed spots were curve fitted to a Gaussian beam model. This algorithm provided the $1/e^2$ irradiance spot size. It also calculated the Gaussian fit which was obtained by performing a chi-squared metric between the measured (quantized) data and the best-fit Gaussian curve [29][30].

The characterization results for the four assembled and pre-aligned OPS barrels is summarized in Table 5. For each barrel, the following information is presented as follows: Average spot size (±0.10μm), average Gaussian fit, and average axial position (±15μm) of (a) the four central spots of an on-axis spot array, and (b) the four corner spots of an on-axis spot array. Note that the average axial position of the corner spots is a direct measure of the field curvature introduced to the on-axis spot array (with the origin set as the average for the four central spots). The measured spot size and Gaussian fit for a corner spot of a 685μm diagonally shifted spot array is also presented (685μm representing the maximum possible lateral shift achievable with the Risley prisms, as will be mentioned later in this secion). The back focal length (i.e. the distance between the last lens surface to the spot array) is given (±0.1mm) for each barrel. The last two columns in table 5 respectively are the spot separation (±0.2μm) and power uniformity (±1.0%). For convenience, the tolerances for the spot size, field curvature, back focal length, spot separation, and power uniformity are written in the headings of the appropriate columns.

It should be noted that any distortion (in spot separation) that was introduced was not measurable within the measurement precision, which is well below the ±0.54μm tolerance for 1% clipping.

Power uniformity of the spot arrays were obtained from a frame-grabbed image using the linear high resolution CCD camera (with automatic gain control turned off). The image was fed into a program which computed the integrated power (in pixel intensity units) per spot by summing the pixel elements within each spot's elementary cell (of 125μm by 250μm). Thus the total integrated power of each spot was measured and compared. This integration was necessary, since it was found to be difficult to match the plane of the spot array to the plane of the CCD active area directly, resulting in a spatially defocused image. Power uniformity measurements for barrels 1 and 2 were unavailable as they had already been integrated into the system. Noting the negligible statistical difference (to within measurement precision) between the measurements for barrels 3 and 4 however, it was expected that the MPGs for barrels 1 and 2 behave similarly, and the power uniformity was better than 92.0%.

Note, from Table 5, that all measurements but two fit within the specified tolerances. The spot size of an outer corner spot of a 685μm diagonally shifted spot array was measured to be 7.04μm for barrel 1, and 6.80μm for barrel 3, both larger than the allowable tolerance. Noting, however, that since the fiber was centered to better than 10μm within the OPS barrel (as presented in SectionV), compared to the ±100μm tolerance (as presented in Section IV), it would only be necessary to laterally shift the spot array by at most ±200μm.

B. Spectral Behavior

Preliminary tests have shown that there was no significant effect caused by the backreflections of the OPS components on the spectral behavior of the laser. The Faraday isolator (figure 4) provided a nominal -40db of isolation and was required to achieve this performance.

C. Polarization

Measurements on the polarization stability of the light from the OPS were conducted. During pre-alignment, an OPS barrel was populated with only the two collimating lenses and the QWP as shown in figure 16. A PBS-QWP assembly (as mentioned in section II) was placed at the output of the OPS. The light transmitted through the PBS-QWP assembly is labelled as P_A and the unwanted leakage light, as P_B.

By using an iterative computer-based active alignment technique fed from a dual-channel power meter, the orientation of the QWP within the OPS barrel was adjusted to produce light that maximized the ratio as given in equation 7:

$$Throughput = \frac{P_A}{P_A + P_B}. \quad (7)$$

Measurements on the throughput through the PBS-QWP assembly was conducted. Maximum light throughput of 95.26% ±0.28% over time was measured using the ratio given in equation 7.

The non-ideal throughput of 95.26% was primarily incurred by the transmission efficiency of the PBS itself (specified to be 96.16% for p-polarization). The remaining 1% loss was due to the finite extinction ratio of the linearly-polarized light emitted from the PM fiber (measured to be 28dB), and imperfect orientation of the QWPs (the one within the OPS, as well as the two attached to the PBS by the supplier). Polarization stability is demonstrated by the ±0.28% time variation of the transmitted light.

D. Beam Steering

Measurement results conducted on the lateral steering travel of the Risley prisms on the spot array were ±685 (±3μm) from the optical axis. Measurement results on the angular steering coverage of the tilt plates were ±0.49°(±0.08°). These values are better than the ±400μm and 0.45° lateral and angular steering requirements as specified in Table 1 to compensate for the alignment errors encountered during the integration of the OPS into the system.

E. Optical Power Budget

Measured throughput efficiencies were conducted on each of the optical elements of the OPS individually with a precision of ±0.05%. The values for barrel 3 are presented in the

third column of Table 4, in relation to their expected (specified) values (column 1) and plotted in figure 17. (Note that the ordinate axis ranges from 65% to 100%). The final column in Table 4 shows the cumulative throughput efficiency after each element based on the measured data from column 3. It is shown that an overall throughput of 73.01% was expected. The overall throughput was measured for barrel 3 and found to be 73.0 ± 0.5%.

VIII. Discussion and Conclusion

It has been shown that an easy to assemble, scalable, robust, compact, and modular optical power supply spot array generator was successfully built to drive an array of 32 Hybrid/SEED modulators for use in a four-stage optical interconnect. The success is based on meeting the specifications which were presented in Table 1. This table is presented again in table 6 along with the characterization results. The power requirement (the seventh item in the list) was satisfied by taking into account measured optical losses encountered by the laser beam through the optical train (figure 4) of 78.6%, and loss at the fiber coupler which was at worst 50%. Based on the laser source providing 500mW, this results in spots at the output of the OPS of 900μW, over 3 times the required power. It should be noted that the optical interconnect, i.e. light originating from the OPS through to the Hybrid/SEED chip on the first stage, through the optics to the Hybrid/SEED chip on the second stage, was established, demonstrating that the requirements for the OPS were satisfied.

Future optical interconnects will most probably employ the use of source based transmitters (e.g. VCSELs) rather than modulators. However, this is only foreseen to occur after the next couple of years. Thus, in the interim, the necessity for the advancement of R&D in this field requires simple, elegant, and practical optical solutions to meet the current state of affairs. This paper has shown that for the first time, a compact modularized spot array generator has been built for use in a modulator based optical interconnect, successfully taking the first step in bridging the generation gap between sophisticated Hybrid/SEED optoelectronics and optics.

IX. Acknowledgment

D. V. Plant was supported by the Canadian Institute for Telecommunications Research under the National Centre for Excellence program of the Government of Canada, by NSERC (#OGP0155159) and FCAR (#NC-1415). This work was also supported by the Nortel/NSERC Chair in Photonic Systems. Acknowledgment is given to the ARPA/CO-OP/Honeywell DOE Workshop for the manufacture of the multiple phase grating. D. J. Goodwill was supported by the Hudson Moore Jr. Chair at the University of Colorado. Appreciation is given to the following for their assistance: George Smith (Heriot-Watt University) who machined a subset of the optomechanics for the optical power supply, Heinz Nentwich (NORTEL) who sawed the multiple phase gratings to chip level accuracy, and special thanks to Don Pavlasek and Joe Boka (McGill University) who not only machined the majority of the optomechanics for the OPS, but provided invaluable assistance in their design. Rajiv Iyer gratefully acknowledges funding from NSERC (PSG-A). Rajiv Iyer also extends gratitude to the entire Photonics Systems Group at McGill University.

X. References

[1] H. S. Hinton, "An Introduction to Photonic Switching Fabrics," Plenum Press, NY (1993).

[2] R. A. Nordin, F. J. Levi, R. N. Nottenburg, J. O'Gorman, T. Tanbun-Ek, and R. A. Logan, "A systems perspective on digital interconnections technology," J. Lightwave Technol. 10, 811—827 (1992).

[3] D. V. Plant, B. Robertson, H. S. Hinton, W. M. Robertson, G. C. Boisset, N. H. Kim, Y. S. Liu, M. R. Otazo, D. R. Rolston, and A. Z. Shang, "An optical backplane demonstrator system based on FET-SEED smart pixel arrays and diffractive lenslet arrays," IEEE Photon Tech. Lett. 7, 1057—1059 (1995).

[4] T. Sakano, T. Matsumoto, and K Noguchi, "Three-dimensional board-to-board free-space optical interconnects and their application to the prototype multiprocessor system—COSINE-III," Appl. Opt. 34, 1815—1822 (1995).

[5] D. Z. Tsang and T. J. Goblick, "Free-space optical interconnection technology in parallel processing systems," Opt. Eng, 33, 1524—1531 (1994).

[6] D. V. Plant, B. Robertson, H. S. Hinton, M. H. Ayliffe, G. C. Boisset, W. Hsiao, D. Kabal, N. H. Kim, Y. S. Liu, M. R. Otazo, D. Pavlasek, A. Z. Shang, J. Simmons, and W. M. Robertson, "A 4 X 4 VCSEL/MSM optical backplane demonstrator system," in *Proceedings of the IEEE-LEOS Annual Meeting 1995* (Institute of Electrical and Electronics Engineers-Lasers and Electro-Optics Society, New York, 1995), Postdeadline paper PD2.4.

[7] D. V. Plant, B. Robertson, H. S. Hinton, M. H. Ayliffe, G. C. Boisset, D. J. Goodwill, D. N. Kabal, R. Iyer, Y. S. Liu, D. R. Rolston, W. M. Robertson, and M. R. Taghizadeh, "A multistage CMOS-SEED optical backplane demonstrator system," Opt. Comput. 96, 14—15 (1996).

[8] F. B. McCormick, F. A. P. Tooley, T. J. Cloonan, J. L. Brubaker, A. L. Lentine, R. L. Morrison, S. J. Hinterlong, M. J. Herron, S. L. Walker, and J. M. Sasian, "Experimental investigation of a free-space optical switching network by using symmetric self-electro-optic-effect devices," Appl. Opt., 31, 5431—5446 (1992).

[9] F. B. McCormick, T. J. Cloonan, A. L. Lentine, J. M. Sasian, R. L. Morrison, M. G. Beckman, S. L. Walker, M. J. Wojcik, S. J. Hinterlong, R. J. Crisci, R. A. Novotny, and H. S. Hinton, "Five-stage free-space optical switching network with field-effect transistor self-electro-optic-effect-device smart-pixel arrays," Appl. Opt., 33, 1601—1618 (1994).

[10] F. B. McCormick, A. L. Lentine, R. L. Morrison, J. M. Sasian, T. J. Cloonan, R. A. Novotny, M. G. Beckman, M. J. Wojcik, S. J. Hinterlong, and D. B. Buchholz, "155 Mb/s operation of a FET-SEED free-space

switching network", Photonics Technology Letters, 6, 1479—1481 (1994).

[11] F. B. McCormick, A. L. Lentine, R. L. Morrison, J. M. Sasian, T. J. Cloonan, R. A. Novotny, M. G. Beckman, M. J. Wojcik, S. J. Hinterlong, and D. B. Buchholz, "Free-space optical switching using FET-SEED smart-pixel arrays", Inst. Phys. Conf. Ser. No 139: Part II, 131—136 (1994).

[12] D. V. Plant, B. Robertson, H. S. Hinton, W. M. Robertson, G. C. Boisset, N. H. Kim, Y. S. Liu, M. R. Otazo, D. R. Rolston, A. Z. Shang, and L. Sun, "A FET-SEED Smart Pixel Based Optical Backplane Demonstrator", Inst. Phys. Conf. Ser. No 139: Part II, 145—148 (1994).

[13] S. Araki, M. Kajita, K. Kasahara, K. Kubota, K. Kurihara, I. Redmond, E. Schenfeld, and T. Suzaki, "Experimental free-space optical network for massively parallel computers", Appl. Opt., 35, 1269—1281 (1996).

[14] K. W. Goosen, J. A. Walker, L. A. D'Asaro, S. P. Hui, B. Tseng, R. Leibenguth, D. Kossives, D. D. Bacon, D. Dahringer, L. M. F. Chirovsky, A. L. Lentine, and D. A. B. Miller, "GaAs MQW modulators integrated with silicon CMOS," IEEE Photon. Technol. Lett., 7, 360—362 (1995).

[15] D. R. Rolston, D. V. Plant, T. H. Szymanski, H. S. Hinton, W. S. Hsiao, M. H. Ayliffe, D. Kabal, M. B. Venditti, P. Desai, A. V. Krishnamoorthy, K. W. Goosen, J. A. Walker, B. Tseng, S. P. Hui, J. C. Cunningham, and

W. Y. Jan, "A hybrid-SEED smart pixel array for a four-stage intelligent optical backplane demonstrator," IEEE Journal of Selected Topics in Quantum Electronics, 2, 97—105 (1996).

[16] B. Robertson, Y. S. Liu, G. C. Boisset, D. J. Goodwill, M. H. Ayliffe, W. H. Hsiao, R. Iyer, D. Kabal, D. Pavlasek, M. R. Taghizadeh, H. S. Hinton, and D. V. Plant, "Optical design and characterization of a compact free-space photonic backplane demonstrator," presented at the *1996 OSA Annual Meeting*, Rochester, NY, paper MLL5 (1996).

[17] G. C. Boisset, M. H. Ayliffe, D. J. Goodwill, B. Robertson, R. Iyer, Y. S. Liu, D. Kabal, D. Pavlasek, W. M. Robertson, D. R. Rolston, H. S. Hinton, and D. V. Plant, "Design, fabrication and characterization of opto-mechanics for a hybrid four-stage free-space optical backplane demonstrator," presented at the *1996 OSA Annual Meeting*, Rochester, NY, paper MBBB4 (1996).

[18] ARPA/AT&T Hybrid SEED Workshop, July 18—21, 1995, George Mason University, Virginia (1995).

[19] IEEE Standard 1014 for a Versatile Backplane Bus: VMEbus (1987).

[20] N. Streibl, "Beam shaping with optical array generators", Journal of Modern Optics, 36, 1559—1573, (1989).

[21] M.P. Dames, R. P. Dowling, P. McKee, and D. Wood, "Efficient optical elements to generate intensity weighted spot arrays", Appl. Opt., 30, 2685—2691 (1991).

[22] A. G. Kirk, and T. J. Hall, "Design of binary computer generated holograms by simulated annealing: coding density and reconstruction error," Optics Communications, 94, 491—496 (1992).

[23] Y.S. Liu, B. Robertson, D. V. Plant, H. S. Hinton, W. M. Robertson, "Design and Characterization of a microchannel optical interconnect for optical backplanes", accepted at Appl. Opt. (1996).

[24] F. B. McCormick, in *Photonics in Switching*, edited by J. E. Midwinter, Academic Press, 1993.

[25] R.E. Fischer and W.J. Smith, "Modern Lens Design - A Resource Manual", McGraw-Hill, pp. 221—238 (1992).

[26] A. C. Walker, I. R. Redmond, D. J. McKnight, R. G. A. Craig, G. S. Buller, P. Meredith, M. R. Taghizadeh, "Construction of an optical cellular logic image processor", SPIE Proceedings, 1806, 373—377, "1992 ICO Topical meeting on optical computing," Minsk, Byelorussia (1992).

[27] R. G. A. Craig, B. S. Wherrett, A. C. Walker, D. J. McKnight, I. R. Redmond, J. F. Snowdon, G. S. Buller, E. J. Restall, R. A. Wilson, S. Wakelin, N. McArdle, P. Meredith, J. M. Miller, M. R. Taghizadeh, G. Mackinnon,

S. D. Smith, "First programmable digital optical processor: optical cellular logic image processor", SPIE Proceedings, 1505, 76—78, "Optics for computer: Architectures and technologies", The Hague, Netherlands (1991).

[28] J. E. Midwinter, "Photonics in switching," Academic Press, pp.200 (1993).

[29] S. Wolfram, "Mathematica - A system for doing mathematics by computer", Addison-Wesley Publishing Company Inc, pp.587, 672 (1991).

[30] P. G. Hoel, "Elementary Statistics", John Wiley & Sons, Inc, pp. 54—67 (1962).

XI. Notes

[A] Delrin[tm] is a trademarked name. The mention of this brand name in this paper is for information purposes only and does not constitute an endorsement of the product by the authors or their institutions.

XII. Tables

OPS Spot array requirement
8 by 4 focused spots on a uniform grid of 125μm (vertical) by 250 μm (horizontal)
8 additional peripheral spots to hit lenslets on LA1 (figure 2)
Spot array positioned between 18.34 ± 0.82mm away from the output of the OPS
$1/e^2$ irradiance spot radii of 6.47μm
Slower than F/6 beams generating spot array
Stable right-hand circularly polarized light
Minimal field curvature of spot array
Power per spot greater than 250μW
Power uniformity across the entire array of greater than 90%.
Beam steering capabilities of better than: ± 400μm lateral translation ± 0.46° angular deviation
Spectral tolerance of 850±1nm

Table 1: OPS Spot Array Requirements

Detailed Design Requirement	Optical/Optomechanical Solution
Spots on a uniform grid	Chose a low distortion Fourier lens
Spot separation matched SEED separation	Adjusted focal length of Fourier lens by changing element separation
$1/e^2$ irradiance spot size of 6.47μm	Adjusted focal length of collimating lens by changing element separation
Collimated beam through the planar elements	Maintained the fiber facet at the front focus of the collimating lens
Wavefront flatness of less than $\lambda/20$	Chose a low aberration Fourier lens; Aberrations from other elements kept low; Maintained fiber at front focus of collimating lens
Angular alignment of spot array about optical axis	Rotated MPG about optical axis
Pitch and yaw alignment of spot array with respect to interconnect	Adjusted the difference in the roll position of the opposed tilt plates
Mutual angular alignment of chief rays of all beams in the spot array	Positioned MPG at front focus of Fourier lens; Chose low distortion Fourier lens
Lateral alignment of spot array	Rotated the Risley prisms about the optical axis

Table 2: Optical and optomechanical degrees-of-freedom

Simulation	Tolerance for 1% clipping	On-axis spot	Corner spot of an on-axis spot array	Spot 1152μm off-axis
Distortion	±2.5μm	0μm	0μm	1.03μm
Field curvature	±63μm	0μm	11.5μm	46μm
Spot size	±0.25μm	6.47μm	6.50μm	6.75μm
Chief ray angle	±0.7°	0°	0.0008°	0.0068°
Strehl ratio	0.8	0.865	0.857	0.817
1/RMS OPD	14	43.2	43.5	28.9

Table 3: Simulation results and tolerance values

Component	Estimated throughput efficiency	Cumulative throughput efficiency	Measured throughput efficiency	Calculated cumulative throughput efficiency based on measured values
Collimating lens 1	99.6%	99.6%	99.24%	99.24%
Collimating lens 2	99.6%	99.2%	99.24%	98.48%
Quarterwave plate	96.8%	96.0%	99.00%	97.50%
MPG	76.5%	73.5%	76.47%	74.56%
Risley prism 1	99.5%	73.1%	99.70%	74.34%
Risley prism 2	99.5%	72.7%	99.70%	74.11%
Tilt plate 1	99.5%	72.4%	99.70%	73.89%
Tilt plate 2	99.5%	72.0%	99.70%	73.67%
Fourier lens 1	99.6%	71.7%	99.55%	73.34%
Fourier lens 2	99.6%	71.4%	99.55%	73.01%

Table 4: Optical power budget characterization results

OPS	Average on-axis center spot			Average on-axis corner spot			Corner spot of a 685μm shifted spot array		BFL	Separ-ation	Power Unif.
	ω	%G	z	ω	%G	z field curv.	ω	%G			
	6.47 ±0.25 μm			6.47 ±0.25 μm		<63 μm	6.47 ±0.25 μm		18.34 ±0.82 mm	125 ±0.54 μm	>90%
1	6.47	93.94	0	6.68	90.64	19.25	7.04	94.05	18.11	124.75	n/a
2	6.61	96.13	0	6.62	96.33	11.50	6.68	95.35	18.00	125.15	n/a
3	6.49	98.13	0	6.47	96.06	38.75	6.80	93.65	18.00	125.15	92.8
4	6.52	94.16	0	6.57	96.03	0.25	6.53	97.00	18.30	124.85	92.9

Table 5: Spot and Spot Array Characterization

OPS Spot array requirement	OPS characterization results for the 4 barrels
8 by 4 focused spots on a uniform grid of 125.00μm by 250.00μm (±0.54μm)	8 by 4 spots on a uniform grid. In vertical direction: min: 124.75μm; max: 125.15μm
8 additional alignment spots	Achieved through MPG design
Back focal length (bfl) of 18.34±0.82mm	Min bfl = 18.00; Max bfl = 18.30
$1/e^2$ irradiance spot radii of 6.47±0.25μm	Min center spot size = 6.47μm Max center spot size = 6.61μm Min corner spot size = 6.47μm Max corner spot size = 6.68μm
Slower than F/6 beams generating spot array	F/12 spots generated
Stable right hand circularly polarized light	Achieved in-situ
Minimal field curvature < 63μm across spot array	Min field curvature = 0.25μm Max field curvature = 38.75μm
Power per spot greater than 250μW	900μW per spot (see Section VIII)
Power uniformity across the entire array of greater than 90%	Array power uniformity >92%
Beam steering capabilities of greater than: ± 400μm lateral translation ± 0.46° angular deviation	Beam steering capabilities of: ±685μm lateral translation ± 0.49° angular deviation
Spectral tolerance of 850±1nm	850.0 ± 0.05nm

Table 6: OPS Spot Array Requirements and Characterization Results

XIII. Figure Captions

XIV. Figures

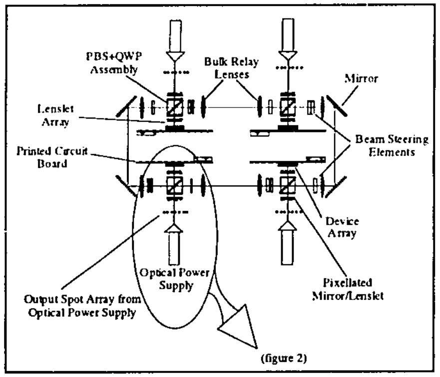

Figure 1: Schematic of the unfolded system

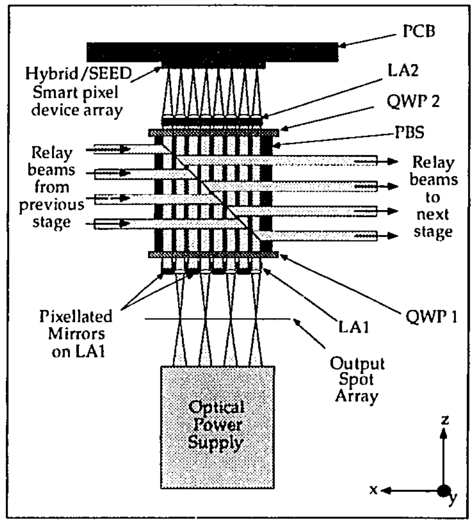

Figure 2: Close-up of one stage

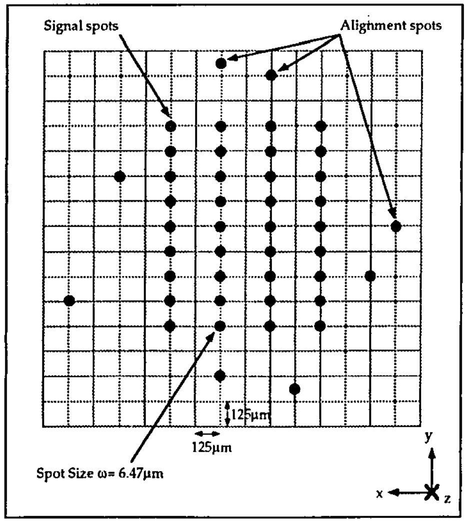

Figure 3: Schematic of desired spot array at the output of the OPS

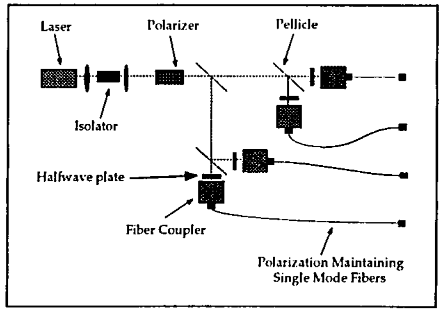

Figure 4: Light distribution system using pellicles

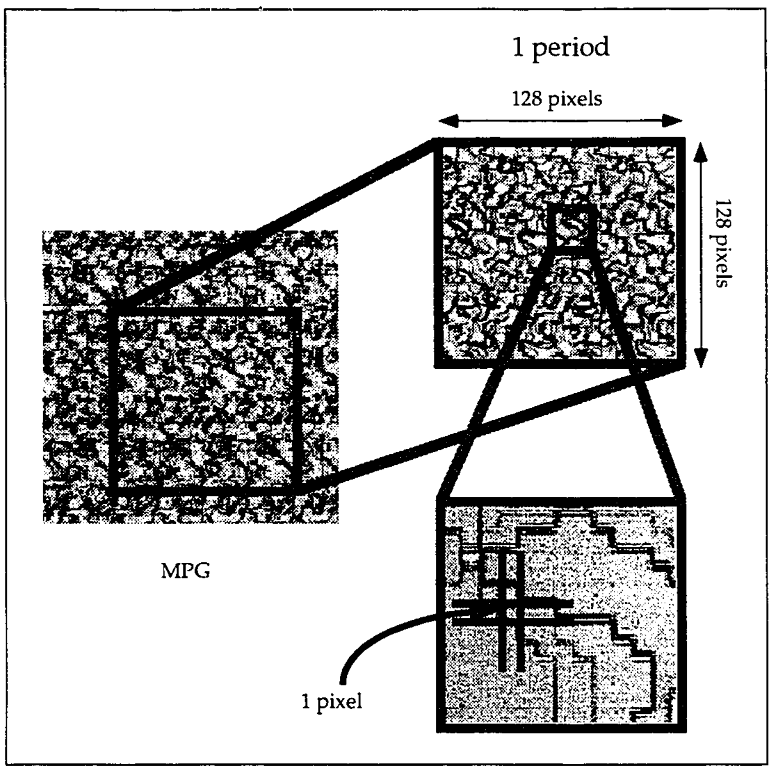

Figure 5: Multiple level phase grating

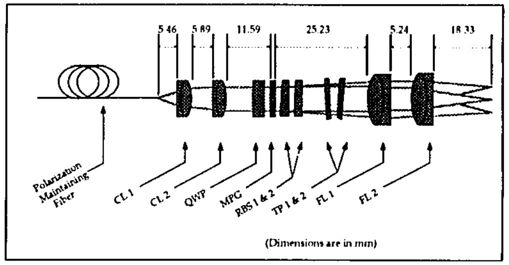

Figure 6: Optical design of the optical power supply

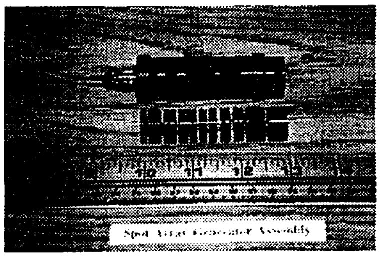

Figure 7: Photo of the unassembled OPS

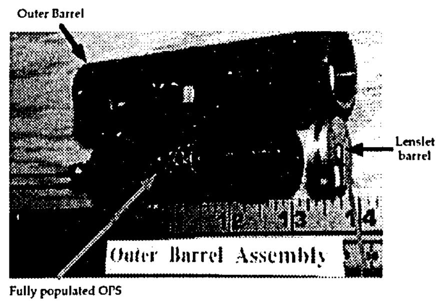

Figure 8: Photo of the fully populated OPS, the outer barre, and the lenslet barrel

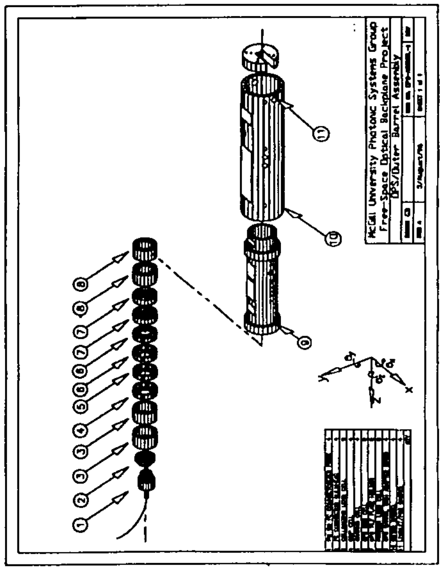

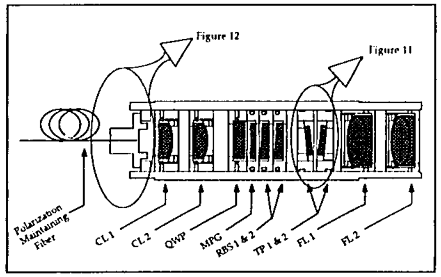

Figure 10: OPS cross-section

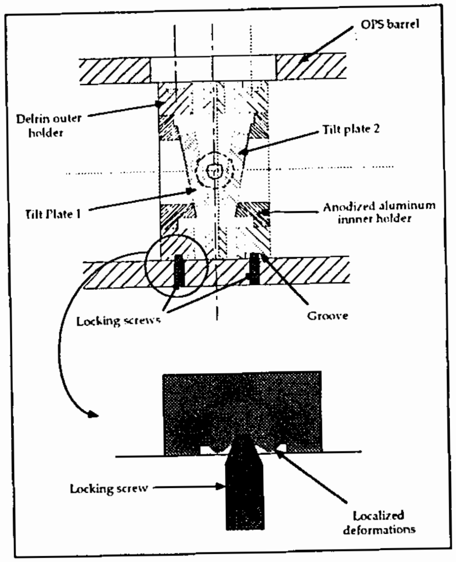

Figure 11: Tilt plate cell design

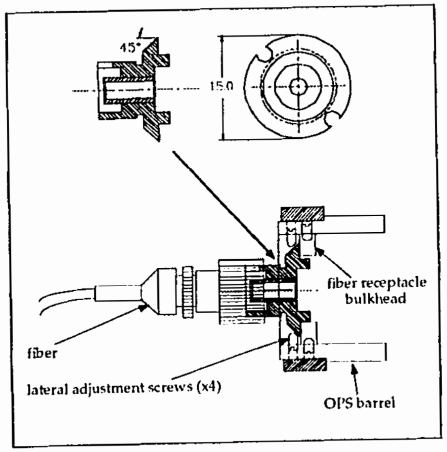

Figure 12: Fiber centering mechanism

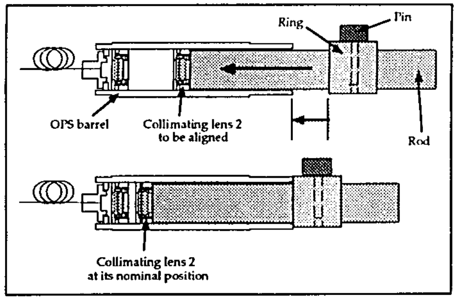

Figure 13: OPS insertion slug

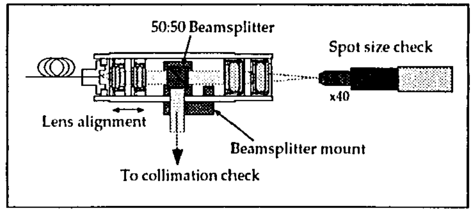

Figure 14: Alignment of the collimating lenses

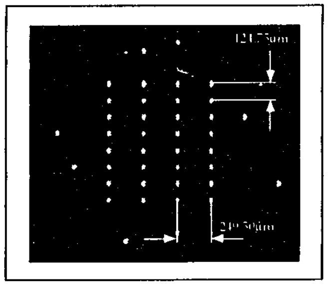

Figure 15: Frame grab of the generated spot array

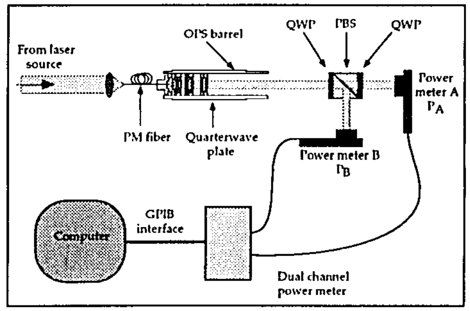

Figure 16: Polarization stability active alignment measurement setup

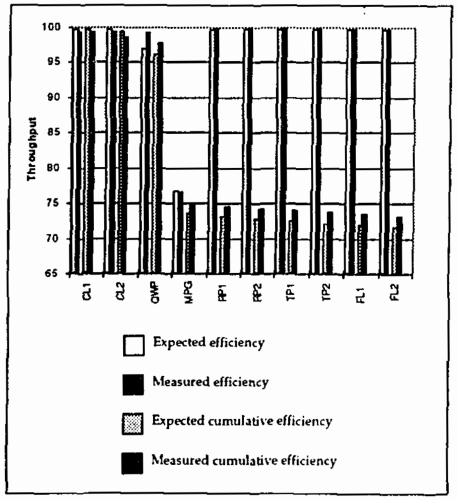

Figure 17 - Plot of the optical power budget